

# Time-resolved diffraction profiles and atomic dynamics in short-pulse laser-induced structural transformations: Molecular dynamics study

Zhibin Lin and Leonid V. Zhigilei\*

*Department of Materials Science and Engineering, University of Virginia, 116 Engineer's Way, Charlottesville, Virginia 22904-4745, USA*

(Received 22 October 2005; revised manuscript received 20 January 2006; published 16 May 2006)

The diffraction profiles and density correlation functions are calculated for transient atomic configurations generated in molecular dynamics simulations of a 20 nm Au film irradiated with 200 fs laser pulses of different intensity. The results of the calculations provide an opportunity to directly relate the detailed information on the atomic-level structural rearrangements available from the simulations to the diffraction spectra measured in time-resolved x-ray and electron diffraction experiments. Three processes are found to be responsible for the evolution of the diffraction profiles. During the first several picoseconds after the laser excitation, the decrease of the intensity of the diffraction peaks is largely due to the increasing amplitude of thermal atomic vibrations and can be well described by the Debye-Waller factor. The effect of thermoelastic deformation of the film prior to melting is reflected in shifts and splittings of the diffraction peaks, providing an opportunity for experimental probing of the ultrafast deformations. Finally, the onset of the melting process results in complete disappearance of the crystalline diffraction peaks. The homogeneous nucleation of a large number of liquid regions throughout the film is found to be more effective in reducing long-range correlations in atomic positions and diminishing the diffraction peaks as compared to the heterogeneous melting by melting front propagation. For the same fraction of atoms retaining the local crystalline environment, the diffraction peaks are more pronounced in heterogeneous melting. A detailed analysis of the real space correlations in atomic positions is also performed and the atomic-level picture behind the experimentally observed fast disappearance of the correlation peak corresponding to the second nearest neighbors in the fcc lattice during the laser heating and melting processes is revealed.

DOI: 10.1103/PhysRevB.73.184113

PACS number(s): 61.80.Az, 78.47.+p, 64.70.Dv, 02.70.Ns

## I. INTRODUCTION

Short (pico- and femtosecond) pulse laser irradiation has the ability to bring material into a highly nonequilibrium state and provides a unique opportunity to study the material behavior and phase transition dynamics under extreme conditions. The challenge of probing fast structural transformations is being met by active development of a variety of time resolved probe techniques.<sup>1–16</sup> Until recently most of the data on the kinetics of laser-induced phase transformations has been provided by optical probe techniques, e.g., Refs. 1–4. While high temporal resolution is readily achievable in optical pump-probe experiments, the reflectivity measured by optical probes can only reveal changes in the electronic structure of the irradiated surface and provides limited direct information on atomic structural rearrangements.

Recent advances in time-resolved x-ray and electron diffraction techniques open up an exciting opportunity to go beyond the analysis of the characteristic time scales of laser-induced phase transformations and to directly probe the transient atomic dynamics. For example, observations of the inertial motion of atoms on the optically modified or softened potential energy landscape, reported by Lindenberg *et al.*,<sup>6</sup> provide new insights into the mechanisms of nonthermal melting of covalently bonded materials. Excitation of large coherent atomic displacements at low laser fluences and disordering or melting at higher fluences has been deduced by Sokolowski-Tinten *et al.* from analysis of time evolution of the diffraction signals obtained for 50 nm bismuth films irradiated with femtosecond laser pulses.<sup>7</sup> The resolidification

process of a laser-melted surface region of an InSb target has been studied with nanosecond temporal resolution by Harbst *et al.* and the velocity of the resolidification front has been measured for different laser fluences.<sup>8</sup> Due to the limited intensity of the available x-ray pulses, the diffraction signals are typically derived from rocking curves, for fixed Bragg angles. The advances in short-pulsed electron sources enable a competitive alternative to x rays in the exploration of atomic dynamics.<sup>9</sup> High structural sensitivity and subpicosecond time resolution were recently demonstrated by Siwick *et al.* in an electron diffraction study of ultrafast solid-to-liquid transition dynamics in 20 nm aluminum films irradiated with 120 fs laser pulses.<sup>11</sup> The diffraction intensity over a range of scattering vectors was measured in this work, allowing for analysis of time evolution of the density correlation function during the melting process and providing information on the atomic rearrangements during the first picoseconds following the optical excitation.

Although time-resolved diffraction experiments provide important atomic-level insights into the fast laser-induced processes, the complexity of the nonequilibrium phase transformations hinders the direct translation of the diffraction profiles to the transient atomic structures. Atomic-level simulations can help in reliable interpretation of experimental observations. Indeed, classical and *ab initio* molecular dynamics (MD) simulations have been used to study the mechanisms and kinetics of laser-induced nonthermal<sup>17,18</sup> and thermal<sup>19–21</sup> melting processes, the evolution of voids in photomechanical spallation,<sup>22</sup> as well as the dynamics of explosive material disintegration and ablation.<sup>23,24</sup> MD simula-

<b>Report Documentation Page</b>			Form Approved OMB No. 0704-0188	
<p>Public reporting burden for the collection of information is estimated to average 1 hour per response, including the time for reviewing instructions, searching existing data sources, gathering and maintaining the data needed, and completing and reviewing the collection of information. Send comments regarding this burden estimate or any other aspect of this collection of information, including suggestions for reducing this burden, to Washington Headquarters Services, Directorate for Information Operations and Reports, 1215 Jefferson Davis Highway, Suite 1204, Arlington VA 22202-4302. Respondents should be aware that notwithstanding any other provision of law, no person shall be subject to a penalty for failing to comply with a collection of information if it does not display a currently valid OMB control number.</p>				
1. REPORT DATE <b>JAN 2006</b>	2. REPORT TYPE	3. DATES COVERED <b>00-00-2006 to 00-00-2006</b>		
4. TITLE AND SUBTITLE <b>Time-resolved diffraction profiles and atomic dynamics in short-pulse laser-induced structural transformations: Molecular dynamics study</b>				
5a. CONTRACT NUMBER				
5b. GRANT NUMBER				
5c. PROGRAM ELEMENT NUMBER				
6. AUTHOR(S)				
5d. PROJECT NUMBER				
5e. TASK NUMBER				
5f. WORK UNIT NUMBER				
7. PERFORMING ORGANIZATION NAME(S) AND ADDRESS(ES) <b>University of Virginia, Department of Materials Science and Engineering, 116 Engineer's Way, Charlottesville, VA, 22904-4745</b>				
8. PERFORMING ORGANIZATION REPORT NUMBER				
9. SPONSORING/MONITORING AGENCY NAME(S) AND ADDRESS(ES)				
10. SPONSOR/MONITOR'S ACRONYM(S)				
11. SPONSOR/MONITOR'S REPORT NUMBER(S)				
12. DISTRIBUTION/AVAILABILITY STATEMENT <b>Approved for public release; distribution unlimited</b>				
13. SUPPLEMENTARY NOTES <b>The original document contains color images.</b>				
14. ABSTRACT				
15. SUBJECT TERMS				
16. SECURITY CLASSIFICATION OF:			17. LIMITATION OF ABSTRACT	18. NUMBER OF PAGES <b>19</b>
a. REPORT <b>unclassified</b>	b. ABSTRACT <b>unclassified</b>	c. THIS PAGE <b>unclassified</b>		19a. NAME OF RESPONSIBLE PERSON

tions provide complete atomic-level information on the mechanisms of laser-induced phase transformations. At the same time, diffraction profiles and density correlation functions can be calculated from atomic configurations predicted in MD simulations, providing a direct connection between the results of MD simulations and time-resolved diffraction experiments.

In this paper we report the results of calculations of diffraction profiles and density correlation functions from transient atomic configurations obtained in MD simulations of short-pulse laser melting of 20 nm Au and Al films. The computational model used in MD simulations of laser melting of metal films is briefly described next, in Sec. II. Numerical methods for calculation of the structure functions from atomic configurations are discussed in Sec. III. The microscopic picture of the competition between the homogeneous and heterogeneous melting processes obtained in MD simulations is discussed and related to the evolution of the diffraction profiles and density correlation functions in Sec. IV. Connections between the characteristic features of the diffraction profiles and the mechanisms of laser melting revealed in the simulations, as well as the implications of the simulation results for interpretation of experimental data are reviewed in Sec. V.

## II. COMPUTATIONAL SETUP FOR SIMULATIONS OF LASER INTERACTIONS WITH Au THIN FILMS

MD simulations of fast laser-induced structural transformations are performed for thin, 20 nm, freestanding metal films irradiated by a short, 200 fs, laser pulse. This choice of the computational system is defined by the availability of high-quality time-resolved electron diffraction data obtained in the transmission mode for thin freestanding films.<sup>10–16</sup> Most of the simulations reported in this paper are for Au films, with an additional simulation performed for an Al film with irradiation conditions comparable to the ones used in a recent experimental study.<sup>11</sup> The simulations are performed with a hybrid atomistic-continuum model that combines the classical MD method for simulation of nonequilibrium processes of lattice superheating, deformation, and melting with a continuum description of the laser excitation and subsequent relaxation of the conduction band electrons. The model is based on well-known two-temperature model<sup>25</sup> (TTM), which describes the time evolution of the lattice and electron temperatures by two coupled nonlinear differential equations. In the combined TTM-MD method, MD substitutes the TTM equation for the lattice temperature. The diffusion equation for the electron temperature is solved by a finite-difference method simultaneously with MD integration of the equations of motion of atoms. The electron temperature enters a coupling term that is added to the MD equations of motion to account for the energy exchange between the electrons and the lattice. The cells in the finite-difference discretization are related to the corresponding volumes of the MD system and the local lattice temperature is defined for each cell from the average kinetic energy of thermal motion of atoms. A complete description of the combined TTM-MD model is given in Ref. 19.

Irradiation by a laser pulse is represented in the continuum part of the model by a source term with a Gaussian temporal profile and exponential attenuation of laser intensity with depth under the surface (Beer-Lambert law). The electron mean free path in Au is larger than the optical penetration depth and the ballistic energy transport defines the effective laser energy deposition depth, estimated to be on the order of 100 nm.<sup>26</sup> Since the ballistic range in Au exceeds the thickness of the films considered in this work, 20 nm, the reflection of the ballistic electrons from the back surface of the film results in a uniform distribution of the electronic temperature established on the time scale of electron thermalization. The theoretical prediction of the uniform rise of the electronic temperature for thicknesses smaller than the ballistic range has been confirmed in a series of pump-probe measurements of transient reflectivity performed for Au films of different thicknesses, from 10 to 500 nm.<sup>27</sup> The effect of the ballistic energy transport and the finite size of the film are accounted for in the source term describing the laser irradiation.<sup>19</sup>

The range of laser fluences used in the simulations performed for Au films, from 45 to 180 J/m<sup>2</sup>, is chosen so that only an incomplete heterogeneous melting of the film is observed at the lowest fluence and an ultrafast homogeneous melting of the whole film is observed at the highest fluence. The absorbed laser fluences rather than the incident fluences are given here and are used in the remaining part of the paper.

The interatomic interaction in the MD part of the model is described by the embedded-atom method (EAM) with the functional form and parametrization suggested in Ref. 28. The choice of the interatomic potential defines all the thermal and elastic properties of the material. Some of the properties of EAM Au relevant to the material response to the laser heating are listed in Table I, along with experimental data for Au. While there are some quantitative discrepancies between the properties of the model EAM Au and experimental data, the overall agreement is reasonable and we can expect that the model will adequately reproduce the material response to fast laser heating. Moreover, the knowledge of the thermodynamic parameters of the model material allows us to perform a quantitative analysis and physical interpretation of the simulation results.

The parameters used in the TTM equation for the electron temperature are as follows. For Au,<sup>19</sup> the electronic heat capacity is  $C_e = \gamma T_e$  with  $\gamma = 71 \text{ J m}^{-3} \text{ K}^{-2}$ , the electron-phonon coupling constant is  $G = 2.1 \times 10^{16} \text{ W m}^{-3} \text{ K}^{-1}$ , and the dependence of the electron thermal conductivity on the electron and lattice temperatures is described by an expression suggested in Ref. 32. For Al,  $C_e = \gamma T_e$  with  $\gamma = 125 \text{ J m}^{-3} \text{ K}^{-2}$ ,  $G = 3.1 \times 10^{17} \text{ W m}^{-3} \text{ K}^{-1}$ ,<sup>33</sup> the electron thermal conductivity is  $K_e = K_0 T_e / T_l$  with  $K_0 = 238 \text{ W m}^{-1} \text{ K}^{-1}$ ,<sup>34</sup> and the optical penetration depth at 800 nm is 8 nm.<sup>12</sup>

The initial MD system in simulations of laser interaction with Au films is a fcc crystal composed of 500 000 atoms with dimensions of  $20.46 \times 20.46 \times 20.46 \text{ nm}^3$  and periodic boundary conditions imposed in the directions parallel to two (001) free surfaces. The periodic boundary conditions simulate the situation in which the laser spot diameter is sufficiently large so that the energy redistribution in the lateral

TABLE I. Some of the material parameters determined for the EAM Au material. Values of the equilibrium melting temperature  $T_m$ , volume change  $\Delta V_m$ , enthalpy  $\Delta H_m$ , and entropy  $\Delta S_m$  of melting are given for zero pressure. The dependence of the equilibrium melting temperature on pressure  $(dT/dP)_m$  is determined from liquid-crystal coexistence simulations and confirmed by the calculations based on the Clapeyron equation  $(dT/dP)_m = \Delta V_m / \Delta S_m$ . The value given in the table is calculated for zero pressure. Variations of the coefficient of linear expansion,  $\alpha$ , and heat capacity at zero pressure,  $C_p$ , are given for a temperature range from 293 to 950 K. Experimental values for Au are from Refs. 29–31.

	$T_m$ (K)	$\Delta V_m$ ( $\text{cm}^3 \text{mol}^{-1}$ )	$\Delta S_m$ ( $\text{J K}^{-1} \text{mol}^{-1}$ )	$\Delta H_m$ (kJ mol $^{-1}$ )	$(dT/dP)_m$ ( $\text{K GPa}^{-1}$ )	$C_p$ ( $\text{J K}^{-1} \text{mol}^{-1}$ )	$\alpha$ ( $10^{-6} \text{K}^{-1}$ )
EAM Au	963	0.28	8.7	8.4	32.2	25.9–30.3	10.3–21.4
Experiment	1336	0.55	9.6	12.8	57.5	25.4–31.2	14.2–19.1
Ref. 29	Ref. 29	Ref. 29	Ref. 29	Ref. 29	Ref. 29	Ref. 30	Ref. 31

directions, parallel to the free surfaces of the film, can be neglected on the time scales considered in the simulations. Several simulations are performed for systems with dimensions of  $8.18 \times 8.18 \times 20.46 \text{ nm}^3$  (80 000 atoms),  $16.37 \times 6.37 \times 20.46 \text{ nm}^3$  (320 000 atoms), and  $28.64 \times 28.64 \times 20.46 \text{ nm}^3$  (980 000 atoms) to investigate the effect of the size of the computational cell on the calculated diffraction profiles. In the simulation performed for an Al film, a similar system composed of 500 000 atoms with dimensions of  $20.56 \times 20.56 \times 20.56 \text{ nm}^3$  is used. Before applying laser irradiation, all systems are equilibrated at 300 K and zero pressure.

The identification of liquid and crystal regions in the atomic configurations obtained in the simulations is done with a local order parameter calculated for each atom based on the local structure within the first two neighbor shells.<sup>19</sup> The local order parameter is used to identify the crystal and liquid regions in the transient atomic configurations and to quantitatively describe the kinetics of the melting process.

### III. NUMERICAL METHODS FOR CALCULATION OF STRUCTURE FUNCTIONS FROM ATOMIC CONFIGURATIONS

In order to calculate diffraction patterns from atomic configurations generated in MD simulations, we consider the scattering of a monochromatic or monoenergetic beam of x-ray photons or electrons on a sample consisting of  $N$  atoms. Assuming that only single elastic scattering takes place, the amplitude of the wave scattered by the sample is given by summing the amplitudes of scattering from each atom in the configuration:<sup>35,36</sup>

$$\Psi_s(\vec{Q}) = \sum_{i=1}^N f_i \exp(-i\vec{Q} \cdot \vec{r}_i), \quad (1)$$

where  $\vec{Q}$  is the scattering vector,  $\vec{r}_i$  is the position of atom  $i$  with respect to an arbitrarily chosen origin,  $f_i$  is the x-ray or electron atomic scattering form factor for the  $i$ th atom, and the sum goes over all the atoms. The magnitude of  $\vec{Q}$  is given by  $Q = 4\pi \sin \theta / \lambda$ , where  $\theta$  is half the angle between the incident and scattered wave vectors, and  $\lambda$  is the wavelength of the incident wave. The scattering form factors  $f_i$  are func-

tions of  $Q$  with different dependences in x-ray and electron scattering.<sup>37</sup> The intensity of the scattered wave can be found by multiplying the scattered wave function by its complex conjugate:

$$I(\vec{Q}) = \Psi_s(\vec{Q}) \cdot \Psi_s^*(\vec{Q}) = \sum_{j=1}^N \sum_{i=1}^N f_i f_j \exp[-i\vec{Q} \cdot (\vec{r}_i - \vec{r}_j)]. \quad (2)$$

The spherically averaged powder-diffraction intensity profile can be obtained by integration of Eq. (2) over all directions of interatomic separation vector  $\vec{r}_{ij} = \vec{r}_i - \vec{r}_j$ , resulting in the Debye scattering equation<sup>35</sup>

$$I(Q) = \sum_{j=1}^N \sum_{i=1}^N f_i f_j \frac{\sin(Qr_{ij})}{Qr_{ij}}. \quad (3)$$

By dividing the above equation by  $\sum_{i=1}^N f_i^2$  we obtain a function that, following Ref. 38, we call the structure function:

$$S(Q) = \frac{I(Q)}{\sum_{i=1}^N f_i^2} = 1 + \frac{2}{\sum_{i=1}^N f_i^2} \sum_{j=1}^N \sum_{i < j} f_i f_j \frac{\sin(Qr_{ij})}{Qr_{ij}}. \quad (4)$$

This function approaches unity at large  $Q$  and is often used to present experimental diffraction results. For a monatomic system the dependence on the atomic form factors can be eliminated and we have

$$S(Q) = 1 + \frac{2}{N} \sum_{j=1}^N \sum_{i < j} \frac{\sin(Qr_{ij})}{Qr_{ij}}. \quad (5)$$

The structure function defined by Eq. (5) can be computed directly from the atomic configurations generated in MD simulations. The calculations, however, involve the summation over all pairs of atoms in the system, leading to the quadratic dependence of the computational cost on the number of atoms and making the calculations prohibitively expensive for large systems.<sup>39</sup>

An alternative approach to calculation of  $S(Q)$  is to substitute the double summation over atomic positions in Eq. (5) by integration over the pair density function, which is a real-space representation of correlations in atomic positions,<sup>38</sup>

$$\rho(r) = \frac{1}{4\pi N r^2} \sum_{j=1}^N \sum_{i=1, i \neq j}^N \delta(r - r_{ij}) = \frac{1}{2\pi N r^2} \sum_{j=1}^N \sum_{i < j}^N \delta(r - r_{ij}) \quad (6)$$

where  $\delta$  is the Dirac delta function. Although the calculation of the pair density function still involves  $N^2/2$  evaluations of interatomic distances  $r_{ij}$ , it can be done much more efficiently than the double summation in Eq. (5), which requires evaluation of the sine function and repetitive calculations for each value of  $Q$ . The expression for the structure function, Eq. (5), can be now reduced to a simple integration, which, in fact, is the Fourier transform of the pair density function:

$$S(Q) = 1 + \int_0^\infty 4\pi r^2 \rho(r) \frac{\sin(Qr)}{Qr} dr. \quad (7)$$

In the calculation of the pair density function, the maximum value of  $r$  is limited by the size of the MD computational cell. If the periodic boundary conditions are used to represent a part of a larger or infinite system, the pair density function can only be evaluated up to a maximum value  $R_{\max}$  that should not exceed one-half of the computational cell. The truncation of the numerical integration in Eq. (7) at  $R_{\max}$  induces spurious ripples with a period of  $\Delta = 2\pi/R_{\max}$ .<sup>40</sup> A number of methods have been proposed to suppress these ripples so that the Fourier ringing dies out more quickly.<sup>35,38,39,41,42</sup> The method that we adopt in this work is to multiply the integrand in Eq. (7) by a damping function  $W(r)$ , similar to the Lorch modification function in neutron diffraction experiments,<sup>43</sup>

$$W(r) = \frac{\sin\left(\frac{r\Delta}{2}\right)}{\frac{r\Delta}{2}} = \frac{\sin\left(\frac{\pi r}{R_{\max}}\right)}{\frac{\pi r}{R_{\max}}}. \quad (8)$$

Thus the structure function  $S(Q)$  can be calculated as

$$S(Q) = 1 + \int_0^{R_{\max}} 4\pi r^2 \rho(r) \frac{\sin(Qr)}{Qr} W(r) dr. \quad (9)$$

The damping function replaces the sharp step function at the cutoff distance  $R_{\max}$  by a smoothly decreasing contribution from the density function at large interatomic distances and eventually approaching zero at  $R_{\max}$ .

Figure 1(a) shows structure functions calculated with and without the damping function for an fcc Au system composed of 500 000 atoms ( $R_{\max}=100$  Å) and equilibrated at 300 K. It is apparent that the introduction of the damping function completely eliminates spurious truncation ripples in the structure function. While for the fcc crystallite at 300 K the presence of ripples does not prevent identification of the real structural peaks, Fig. 1(a), the elimination of ripples is crucial for the analysis of the structural transformations occurring at elevated temperatures, when the real structural peaks can be small and completely obscured by the ripples.

Although application of the damping function eliminates the truncation ripples, the finite size of the MD system and the introduction of the cutoff in the pair density function also

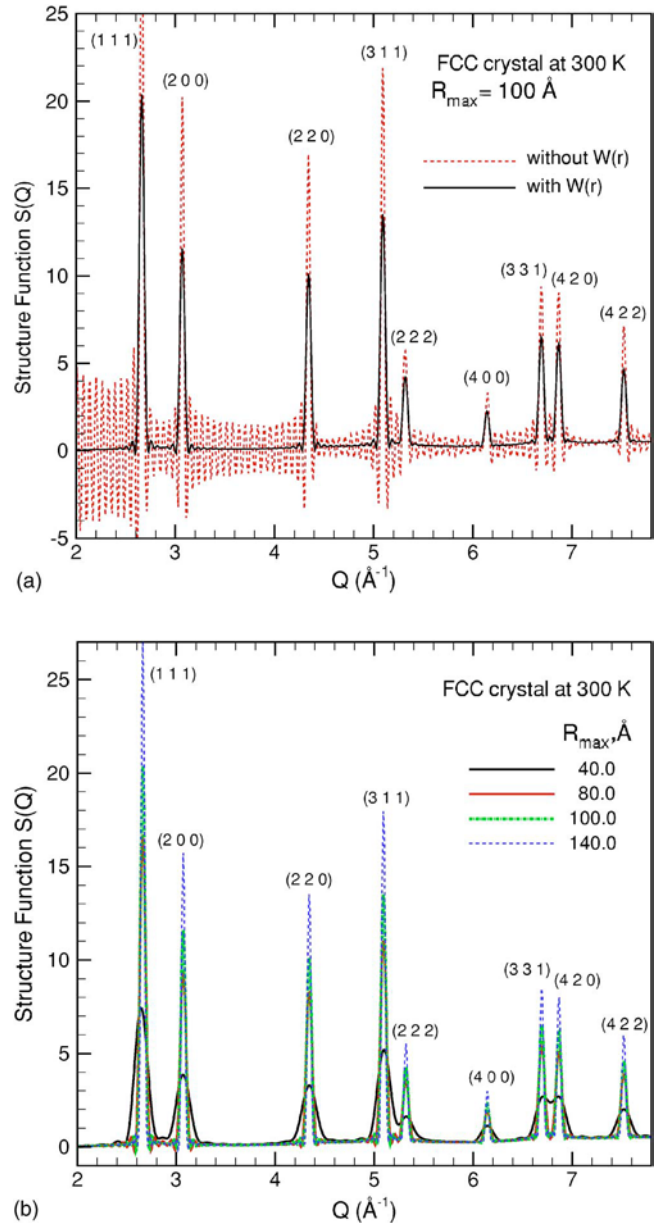


FIG. 1. (Color online) The effect of the finite size of the MD system on the calculated structure functions. Elimination of spurious ripples induced by the truncation of the pair density function at  $R_{\max}=100$  Å by introduction of the damping function  $W(r)$  in Eq. (9) is illustrated in (a), where the results are shown for a  $20.46 \times 20.46 \times 20.46$  nm<sup>3</sup> fcc Au system equilibrated at 300 K. Solid (black) and dashed (red) lines show the results of the calculations performed with and without  $W(r)$ , respectively. Structure functions calculated using Eq. (9), with the damping function, for systems of four different sizes in the lateral directions are shown in (b).

affect the real peaks of the structure function. To illustrate the effect of the size of the system on the characteristics of structure function, the results of calculations performed for a 20-nm-thick Au film represented by MD computational cells with four different sizes in the directions of periodic boundary conditions, parallel to the surfaces of the film, 8.18, 16.37, 20.46, and 28.64 nm are shown in Fig. 1(b). The cutoff distances  $R_{\max}$ , used in the calculations of the pair density

functions are 40, 80, 100, and 140 Å, respectively. It can be seen that the failure to include long-range atomic correlations beyond 40 Å results in a significant broadening of all peaks, with some of the peaks starting to merge. As the value of  $R_{\max}$  increases to 80 Å, the peaks become sharp and well defined. Further increase of  $R_{\max}$  to 100 and to 140 Å results in a much more moderate sharpening of the peaks, with no changes to the peak positions. Analytical calculation of the broadening of the peaks due to the introduction of the damping function with  $R_{\max}=100$  Å predicts a broadening of  $\Delta Q=5.437/R_{\max}=0.05437$  Å<sup>-1</sup>.<sup>44</sup> Since the purpose of the present paper is to investigate the evolution of the diffraction pattern during the fast laser heating of the film up to the melting temperature and above, the relatively small finite-size effect is expected to be negligible compared to the changes in the diffraction peaks associated with the temperature rise and structural transformations. Thus, all simulations discussed in the next section are performed for a 20.46 × 20.46 × 20.46 nm<sup>3</sup> (500 000 atoms) system and all structure functions are calculated with Eq. (9) and  $R_{\max}=100$  Å.

#### IV. RESULTS AND DISCUSSION

##### A. Kinetics and mechanisms of laser melting

The time scales of laser melting predicted in TTM-MD simulations of 20 nm Au films irradiated with 200 fs laser pulses at absorbed fluences ranging from 45 to 180 J/m<sup>2</sup> are presented in Fig. 2. The fraction of the crystal phase is defined by the number of atoms with local crystalline environment, as predicted by the local order parameter.<sup>19</sup> Two distinct regimes can be identified in Fig. 2, a high-fluence regime when the entire film melts within just several picoseconds, and a low-fluence regime when the melting process slows down and the melting starting time increases sharply with decreasing fluence. Below we briefly discuss the melting mechanisms of Au films in these two regimes.

At the highest laser fluence of 180 J/m<sup>2</sup>, melting starts at about 10 ps after the laser pulse and completes by 14 ps. Similarly fast decrease of the fraction of the crystal phase is observed in simulations performed at absorbed fluences of 140 and 100 J/m<sup>2</sup>. The melting mechanism in this high-fluence regime is exemplified here by the results obtained in a simulation performed at 180 J/m<sup>2</sup>. The temporal and spatial evolution of the lattice temperature and pressure in the irradiated film is shown in the form of contour plots in Fig. 3. The large mean free path of excited electrons and a weak electron-phonon coupling in Au results in a uniform distribution of the electronic temperature in the film before the electron-lattice thermalization. As a result the whole film is heated up uniformly at a rate on the order of ∼10<sup>14</sup> K/s [Fig. 3(a)]. The fastest heating is observed within the first 15 ps of the simulation, whereas complete equilibration between the hot electrons and the lattice takes up to 70 ps. The fast increase of the lattice temperature results in the overheating of the lattice above the limit of its stability, ∼1.25 $T_m$ ,<sup>19</sup> and leads to the fast homogeneous melting of the whole film within ∼3–4 ps. The solid and dashed lines in Fig. 3 mark the beginning (90% of the crystal phase) and the end (10% of

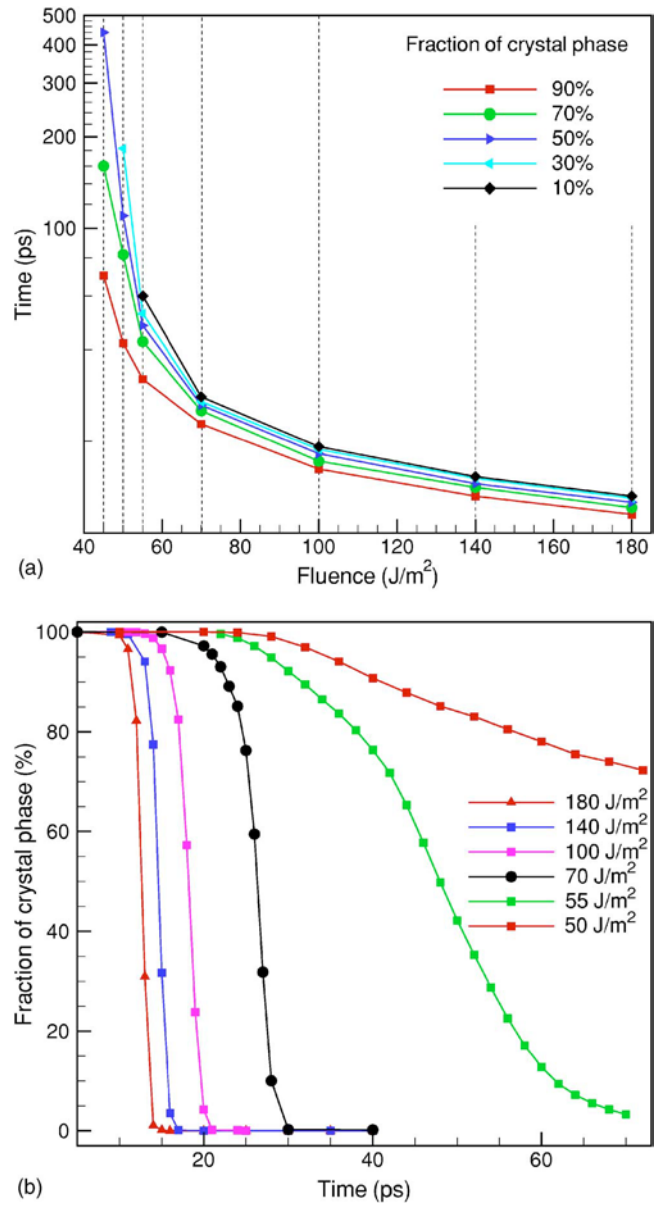


FIG. 2. (Color online) The time scales of the melting process in a 20 nm Au film irradiated with a 200 fs laser pulse at different absorbed fluences. Semilogarithmic plots of the time required to melt certain fractions of the film are shown in (a). Each curve corresponds to a particular fraction of the remaining crystal phase as a function of the absorbed fluence. For example, the (red) curve with squares corresponds to the time after laser excitation when 90% of the atoms in the film belong to the crystal phase. The decrease of the fraction of the crystal phase with time is shown for each simulation in (b). The atoms in the crystal phase are distinguished from the ones in the liquid phase based on the local order parameter (Ref. 19).

the crystal phase) of the melting process and can be related to the corresponding points in Fig. 2.

The pressure contour plot in Fig. 3(b) shows that the fast lattice heating results in the buildup of compressive stresses inside the film within the first ∼5 ps. The initial compressive pressure drives the expansion of the film. In earlier simulations performed for Ni and thicker Au films<sup>19,20,45</sup> the relax-

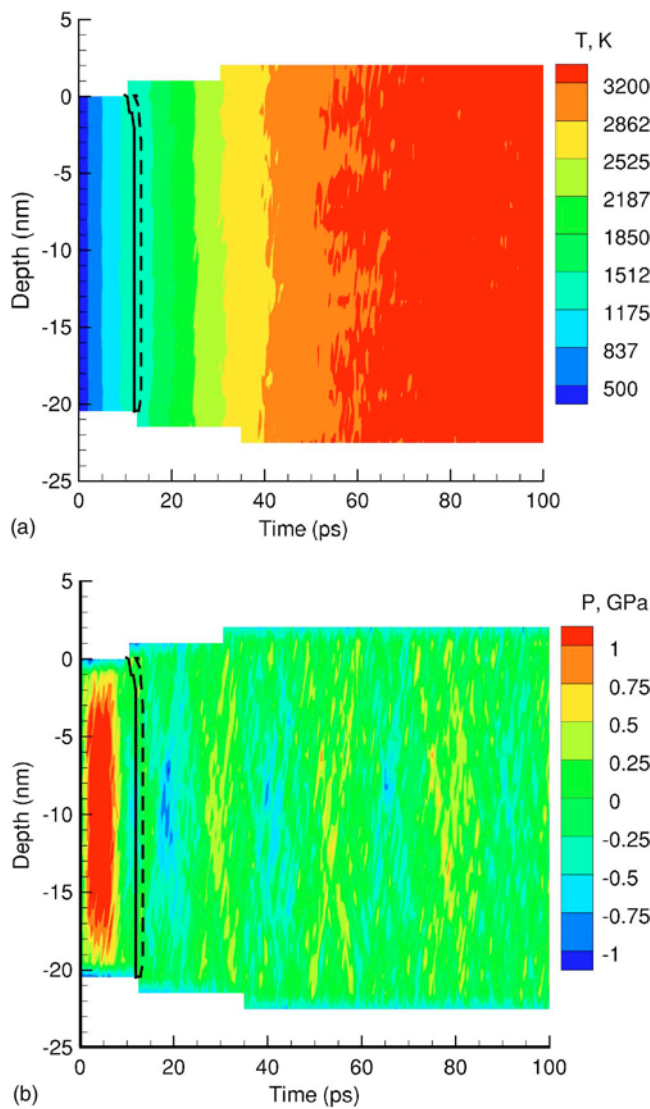


FIG. 3. (Color online) Contour plots of the lattice temperature (a) and pressure (b) for a simulation of laser melting of a 20 nm Au film irradiated with a 200 fs laser pulse at an absorbed fluence of 180 J/m<sup>2</sup>. Solid and dashed lines show the beginning and the end of the melting process. Laser pulse is directed along the *Y* axes, from the top of the contour plots. The stepwise shape of the contour plot boundaries is related to the discretization of the mesh over which average temperature and pressure values are calculated.

ation of the laser-induced compressive stresses resulted in generation of tensile stresses, followed by pressure oscillations or even disintegration of the film. For a 20 nm free-standing Au film, however, the time of the mechanical relaxation is on the order of 5 ps (time needed for two unloading waves propagating from the free surfaces of the film to cross one half of the depth of the film), significantly shorter than the time of the lattice heating. As a result, the film expands during the lattice heating and pressure (and film thickness) oscillations can be hardly observed in Fig. 3(b).

The atomic-level picture of the homogeneous melting process in the high-energy regime is shown in Fig. 4(a). The visual analysis of snapshots from the simulation suggests that the growth of the liquid regions appearing at the free

surfaces of the film (see a snapshot taken at 10 ps) does not make any significant contribution to the overall melting process. The energy transfer from the hot electrons to the lattice quickly leads to the overheating of the lattice up to the limit of the crystal stability, when a spontaneous nucleation of a large number of small liquid regions occurs throughout the film, leading to the rapid collapse of the crystalline structure from 10 to 14 ps.

A similar melting process, dominated by homogeneous nucleation of liquid regions inside the overheated crystal, is observed for all other fluences in the high-fluence regime, down to 70 J/m<sup>2</sup>. The decrease in fluence shifts the melting process to a later time and gradually increases the contribution of the heterogeneous melting that takes place by propagation of two melting fronts from the surfaces of the film. The latter process is reflected in the development of the initial slow shoulders in the melting curves shown in Fig. 2(b). The slow components of the melting process are apparent in the curve plotted for 70 J/m<sup>2</sup>, where almost 10% of the film melts due to the propagation of the melting fronts, before the critical superheating is reached and the faster homogeneous melting takes over.

The melting process observed at 55 J/m<sup>2</sup> can be considered to be a transitional one between the high-fluence (homogeneous melting) and low-fluence (heterogeneous melting) regimes. At this fluence both mechanisms of melting contribute approximately equally to the melting process [Fig. 5(a)]. During the time from 25 to 40 ps, the propagation of two melting fronts from the surfaces of the film is largely responsible for the increase in the fraction of the liquid phase. After 40 ps, the growth of liquid regions nucleated inside the overheated crystal starts to make a major contribution to the melting process, significantly accelerating the total rate of melting, as reflected in the slope of the melting line in Fig. 2(b). The melting slows down again at later time due to the lattice temperature decrease. From the time of 70 to 90 ps the last crystalline island slowly melts [Fig. 5(a)], as the temperature of the film is approaching the equilibrium melting temperature.

At laser fluences below 55 J/m<sup>2</sup>, the propagation of the melting fronts from the surfaces of the film dominates the melting process and a significant increase of the melting time is observed in Fig. 2. Snapshots from a simulation performed at a fluence of 45 J/m<sup>2</sup> illustrate the melting process in this regime [Fig. 6(a)]. Two melting fronts propagate from the free surfaces with velocities that decrease down to zero as the melting progresses and the temperature approaches the equilibrium melting temperature. By the end of the simulation (500 ps) the temperature of the film decreases down to the equilibrium melting temperature and the remaining 49% of the film material remains in the crystalline state. Incomplete and purely heterogeneous melting is also observed in the simulations performed at 50 and 51 J/m<sup>2</sup>. Based on the properties of the model EAM Au material we can estimate the critical absorbed fluence  $F_m$  that would supply enough energy to completely melt the film:

$$F_m = \left( \int_{300}^{T_m} C_l(T) dT + \int_{300}^{T_m} C_e(T) dT + \Delta H_m \right) d, \quad (10)$$

where  $d$  is the thickness of the film,  $C_l$  and  $C_e$  are the lattice

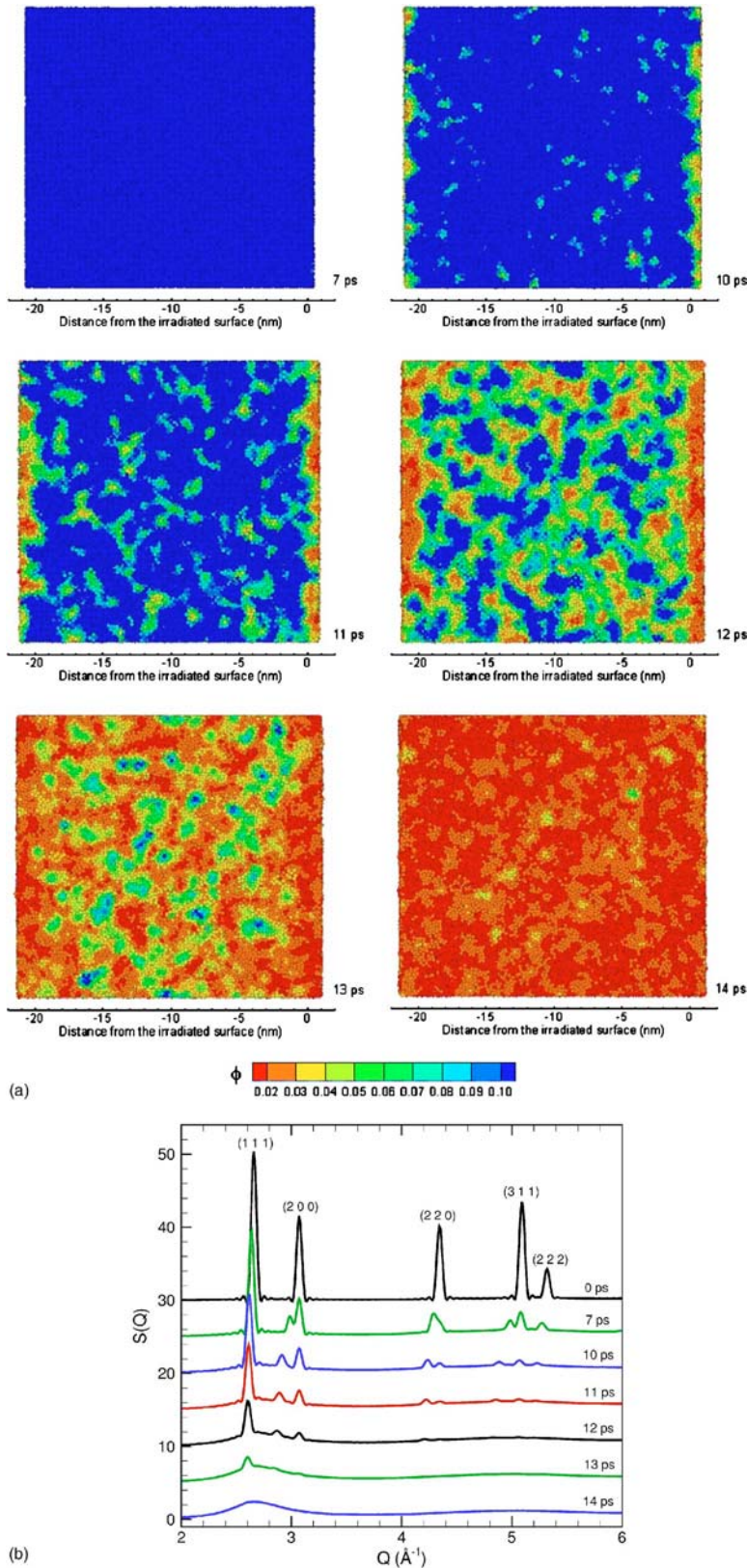


FIG. 4. (Color online) Snapshots (a) and structure functions (b) of atomic configurations during the melting process in a 20 nm Au film irradiated with a 200 fs laser pulse at an absorbed fluence of  $180 \text{ J/m}^2$ . Atoms are colored according to the local order parameter  $\phi$ —blue atoms have local crystalline surroundings, red atoms belong to the liquid phase. In (a), the laser pulse is directed from the right to the left sides of the snapshots. In (b), curves are shifted vertically with respect to each other in order to better show the changes in the structure function. Zero time corresponds to a perfect fcc crystal at 300 K just before the laser irradiation.

and electron heat capacities, and  $\Delta H_m$  is the heat of melting. Using the parameters of EAM Au listed in Table I and electron heat capacity defined in Sec. II we can estimate  $F_m = 53.78 \text{ J/m}^2$ , with  $36.52$  and  $0.59 \text{ J/m}^2$  going into heating of the lattice and electrons up to the equilibrium melting

temperature  $T_m$  and  $16.67 \text{ J/m}^2$  required for melting the film at  $T_m$ . This estimation is consistent with the results of MD simulation described above.

The relative contribution of the homogeneous and heterogeneous melting mechanisms in the simulations described

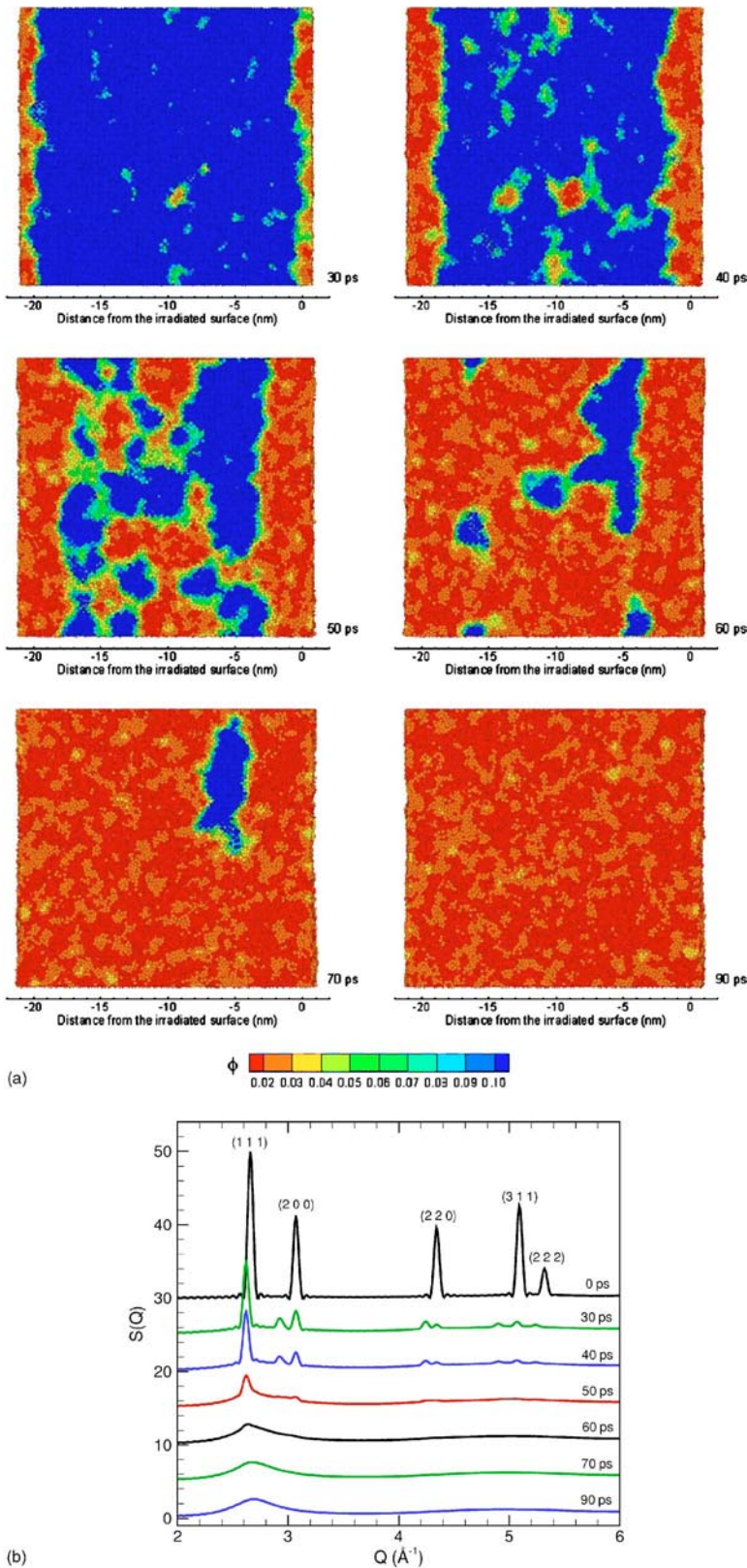


FIG. 5. (Color online) Snapshots (a) and structure functions (b) of atomic configurations during the melting process in a 20 nm Au film irradiated with a 200 fs laser pulse at an absorbed fluence of  $55 \text{ J/m}^2$ . Atoms are colored according to the local order parameter  $\phi$ —blue atoms have local crystalline surroundings, red atoms belong to the liquid phase. In (a), the laser pulse is directed from the right to the left sides of the snapshots. In (b), curves are shifted vertically with respect to each other in order to better show the changes in the structure function. Zero time corresponds to a perfect fcc crystal at 300 K just before the laser irradiation.

above is controlled by the temperature dependence of the velocity of the melting fronts propagating from the free surfaces of the film and the lattice heating regime. The rate of the lattice heating is defined by the irradiation parameters (laser fluence and pulse duration) and the strength of the

electron-phonon coupling, whereas the temperature dependence of the velocity of the melting front can be described by nonequilibrium kinetic theory.<sup>46</sup> The maximum velocity of the melting front propagation is the velocity at the limit of the crystal stability, above which a massive homogeneous

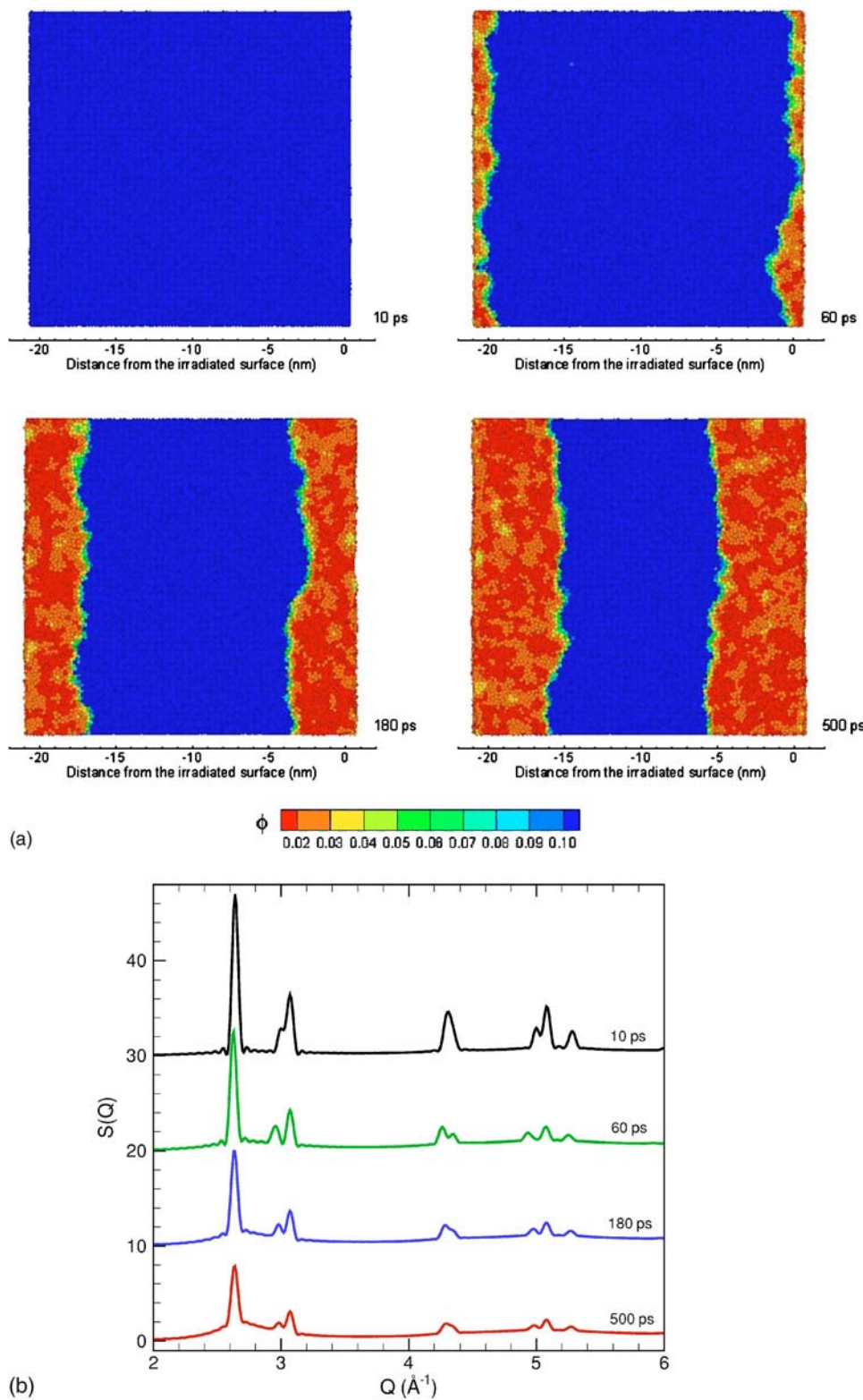


FIG. 6. (Color online) Snapshots (a) and structure functions (b) of atomic configurations during the melting process in a 20 nm Au film irradiated with a 200 fs laser pulse at an absorbed fluence of 45 J/m<sup>2</sup>. Atoms are colored according to the local order parameter  $\phi$ —blue atoms have local crystalline surroundings, red atoms belong to the liquid phase. In (a), the laser pulse is directed from the right to the left sides of the snapshots. In (b), curves are shifted vertically with respect to each other in order to better show the changes in the structure function.

nucleation of liquid regions inside the overheated crystal takes place. While one can safely assume that the maximum velocity of the melting front is ultimately limited by the speed of sound,<sup>47</sup> recent MD simulations<sup>19</sup> demonstrate that the real maximum velocity at the limit of crystal stability does not exceed 15% of the speed of sound. Moreover, under conditions of laser melting, the overheating required for the

onset of the homogeneous nucleation of liquid regions is significantly reduced by the uniaxial lattice distortions produced as a result of the relaxation of laser-induced thermoelastic stresses.<sup>20</sup> This reduction in the lattice stability explains why the homogeneous nucleation is observed down to a relatively low fluence of 55 J/m<sup>2</sup>, when the melting process is slow and takes up to 90 ps.

### B. Structure function calculations

Calculation of the diffraction profiles provides an attractive possibility to directly relate the detailed information on the kinetics and mechanisms of laser-induced structural transformations obtained in MD simulations to the results of time-resolved diffraction experiments.<sup>5–8,10–13</sup> In this section we present the results on the evolution of the structure function  $S(Q)$  in two representative simulations discussed above, a simulation at  $180 \text{ J/m}^2$  where a fast homogeneous melting is observed and a simulation at  $45 \text{ J/m}^2$  where much slower heterogeneous melting takes place.

The temporal evolution of the diffraction profile is shown for a fluence of  $180 \text{ J/m}^2$  in Fig. 4(b). Although by the time of 7 ps the melting process has barely started and most atoms ( $\sim 99\%$ ) are still identified by the local order parameter as maintaining local crystalline surroundings, the structure function has changed significantly. First, there is a considerable reduction in the heights of all the peaks as compared to the structure function calculated at zero time, before the laser pulse. This reduction can be largely attributed to the fast heating of the crystal from 300 to 1059 K [Fig. 3(a)]. Quantitative analysis of peak height reduction due to the increase in the amplitudes of thermal atomic vibrations is given in Sec. IV D. Second, there is a pronounced shift to the left of the (111) diffraction peak and splitting of the (200), (220), and (311) peaks. The appearance of new diffraction peaks may be indicative of solid-solid phase transformations. A detailed structural analysis, however, does not reveal any structural changes in the film beyond the appearance of a relatively small number of point defects (vacancy-interstitial pairs). Both the shift and the splitting of the peaks are actually related to the uniaxial expansion of the film in response to the laser heating, as explained in Sec. IV C.

A fast collapse of the crystalline structure from 10 to 14 ps, apparent from the snapshots shown in Fig. 4(a), is also clearly reflected in the evolution of the structure function. In just 3–4 ps the peaks characteristic of the fcc structure disappear and the structure function takes the shape characteristic of the liquid structure, with only one broad peak that can be identified. The duration of the melting process observed in this simulation is in a good agreement with the one measured in time-resolved electron diffraction experiments performed for 20 nm Al films, 3.5 ps.<sup>11</sup> Some of the differences between the evolution of the diffraction peaks observed in the simulation and experiment, most notably the absence of peak splitting and shifts in the positions of diffraction peaks in experimental observations, are discussed in Sec. V.

An evolution of the structure function in the low-fluence regime, when the melting process is dominated by the propagation of the melting fronts from the free surfaces of the film, is illustrated in Fig. 6(b), where the results are shown for an absorbed fluence of  $45 \text{ J/m}^2$ . Similarly to the fast homogeneous melting discussed above, laser irradiation leads to the reduction of heights of the peaks and induces a shift of the (111) peak to the left and splitting of other peaks. There are, however, important differences in the evolution of the structure functions in low- and high-energy regimes. While the heights of the peaks are decreasing gradually dur-

TABLE II. Fraction of atoms with local crystalline surroundings (local order parameter  $\phi > 0.04$ ) in a 20 nm Au film irradiated with a 200 fs laser pulse at absorbed fluences of 45 and  $180 \text{ J/m}^2$ .

Absorbed fluence = $45 \text{ J/m}^2$				
Time (ps)	10	60	180	500
Crystal fraction (%)	100.0	93.1	67.5	49.1
Absorbed fluence = $180 \text{ J/m}^2$				
Time (ps)	11	12	13	14
Crystal fraction (%)	93.1	67.5	15.9	0.3

ing the melting process, the peaks remain well defined up to the end of the simulation, when more than 50% of the film is melted. For the same fraction of atoms belonging to the crystalline parts of the system (having crystalline local environment as defined by the local order parameter) the diffraction peaks are more pronounced in the case of heterogeneous melting. For instance, although from Table II we can see that the same number of atoms remain in the crystalline parts of the film at 11 ps after the  $180 \text{ J/m}^2$  pulse and at 60 ps after the  $45 \text{ J/m}^2$  pulse, the diffraction peaks are much more clearly defined in the corresponding curve in Fig. 6(b), as compared to the one in Fig. 4(b). One can derive the same conclusion from the comparison of structure functions shown for 12 ps in Fig. 4(b) and 180 ps in Fig. 6(b).

It is clear from the visual analysis of the snapshots of atomic configurations that the homogeneous nucleation of a large number of liquid regions throughout the film [Fig. 4(a)], is effective in destabilizing the lattice and reducing the long-range order throughout the film. While most of the atoms still retain their local crystalline surroundings at 11 and 12 ps, the long-range correlations in atomic positions are largely lost and the diffraction peaks are significantly reduced. Similarly, the presence of relatively small crystalline islands observed at 60 and 70 ps in a simulation performed at  $55 \text{ J/m}^2$  [Fig. 5(a)] can be hardly identified from the corresponding diffraction patterns [Fig. 5(b)]. In the case of heterogeneous melting, the correlations in atomic positions are retained on the scale of the crystalline regions and the diffraction pattern is generated by superposition of the diffraction from the liquid and crystalline parts of the system. In other words, the long-range order is more subtle in homogeneous melting than in heterogeneous melting due to the smaller characteristic length scales at which the homogeneous phase transformation takes place.

### C. Splitting of the peaks: The uniaxial lattice expansion

In this section we discuss the splitting of the diffraction peaks that takes place shortly after the laser irradiation [Figs. 4(b), 5(b), and 6(b)] and demonstrate that the splitting is a direct consequence of the uniaxial thermoelastic deformation of the film in response to the laser heating.

Laser excitation of the conduction band electrons and following electron-phonon equilibration lead to the fast heating of the lattice [Fig. 3(a)] and generation of thermoelastic stresses [Fig. 3(b)], which drive the expansion of the film.

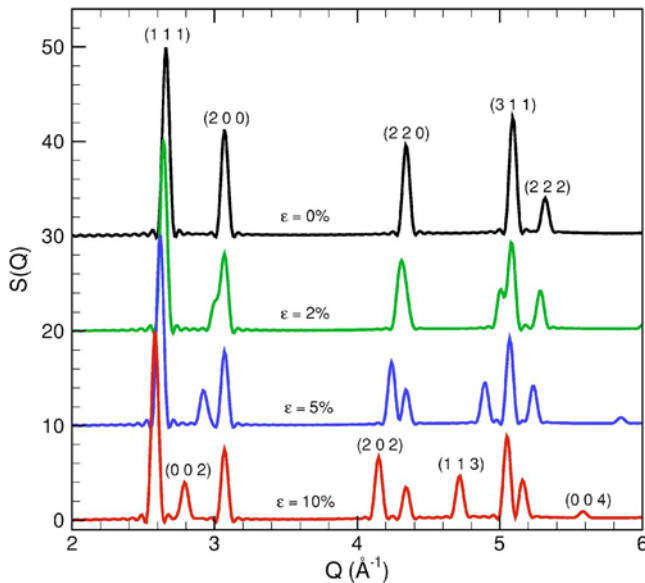


FIG. 7. (Color online) Structure functions of atomic configurations generated by uniform uniaxial deformation of a 20 nm Au fcc film in the direction normal to the free (001) surfaces. The values of the deformation are indicated in the figure. Temperature of the film is 300 K. Curves are shifted vertically with respect to each other in order to better show the changes in the structure function. Structure peaks are identified by Miller indices.

The periodic boundary conditions applied in the directions parallel to the surfaces of the film only allow the expansion of the film to proceed in the direction normal to the surface. These conditions of the lateral confinement are also realized in experiments, where the laser spot diameter is much larger than the depth of the heated region or thickness of the irradiated film. The simulations are performed for a single-crystalline fcc film with (001) free surfaces. The uniaxial deformation of the fcc lattice along the [001] direction changes the space group symmetry of the lattice as the cubic lattice transforms into a tetragonal lattice. Thus, one should expect the occurrence of new diffraction peaks corresponding to the face-centered tetragonal (fct) lattice.

In order to investigate the degree to which the lattice expansion alone can explain the splittings observed in the diffraction profiles in Figs. 4(b), 5(b), and 6(b), we calculate structure functions for a series of Au fcc structures uniaxially deformed along the [001] direction. The results of the diffraction profile calculations are shown in Fig. 7. Splittings and shifts of the diffraction peaks, increasing with increasing deformation, are apparent in the figure. The diffraction peaks from (111) and (311) atomic planes, present in the original fcc structure, shift in the direction of smaller  $Q$ . New diffraction peaks with (002), (202), (113), and (004) Miller indices appear as the lattice transforms from fcc to fct.

It should be noted that the appearance of new peaks is not observed in MD simulations of a fcc crystal slowly heated up to the melting temperature under constant hydrostatic pressure conditions (with periodic boundary conditions applied in all directions). In these simulations the effects of an increase in temperature are limited to the decrease of the heights of the peaks due to the atomic thermal vibrations (see

Sec. IV D) and shift of the peak positions to smaller values of  $Q$  due to the isotropic thermal expansion of the crystal.

By comparing the diffraction profiles obtained for the uniaxially deformed films (Fig. 7) with the results obtained in the laser melting simulations [Figs. 4(b), 5(b), and 6(b)], we can conclude that both the shifts and splittings of the peaks can be explained by the uniaxial thermoelastic expansion of the lattice. Using the (002) peak splittings shown in Fig. 7 as a reference, we can estimate that uniaxial deformations along the (001) direction of 2.8%, 5.3%, and 6.6% would produce the values of peak shifts and splittings observed in a simulation performed at 180 J/m<sup>2</sup> [Fig. 4(b)] at 7, 10, and 11 ps, respectively. These values calculated from the diffraction spectra are consistent with the ones obtained by directly measuring the thickness of the film in the snapshots of the atomic configurations [Fig. 4(a)] as well as with the distances between the density peaks in the density distribution along the direction normal to the film surfaces. The distances between the density peaks correspond to the spacing between the (001) lattice planes in the expanded film and are directly related to the position of the (002) diffraction peak.

In the case of the absorbed fluence of 45 J/m<sup>2</sup> (Fig. 6), the splittings of the diffraction peaks at 10, 60, 180, and 500 ps correspond to 2.3%, 3.9%, 3.1%, and 3.1% uniaxial deformations of the lattice. These values are again consistent with interplane distances measured in the density distribution along the direction normal to the film surfaces. The direct measurement of deformation based on the thickness of the film is hampered in this case by melting of the surface regions. The diffraction profiles calculated for times of 180 and 500 ps show some subtle reverse shifts and decrease in the splittings of the peaks with respect to the shift values observed at 60 ps. These changes may be related to the gradual cooling of the film associated with the melting process, by ~50 K from 60 to 180 ps.

Thus, the results discussed above indicate that, in the fluence range considered in this study, the melting of Au film is preceded by a significant thermoelastic uniaxial lattice expansion, which can be identified from shifts and splittings of the diffraction peaks. It has been shown that the uniaxial expansion and associated anisotropic lattice distortions can significantly reduce the lattice stability against the initiation of melting and can lead to the homogeneous nucleation of liquid regions at temperatures close to the equilibrium melting temperature.<sup>20</sup> Although the analysis performed in this paper is done for a single-crystal film oriented perpendicular to [001] direction, quantitative analysis of laser-induced deformations is also possible for polycrystalline samples, as soon as the texture of the sample is known, e.g., Ref. 48. Investigation of the development of thermoelastic deformations in time-resolved x-ray or electron diffraction experiments has a potential for providing important information on the characteristic time scale of lattice heating and thermoelastic deformation as well as on the role of the uniaxial deformation in laser-induced phase transformations. Indeed, the evolution of the lattice deformation in a Au(111) single crystal following short-pulse laser heating has been measured with ~10 ps temporal resolution in x-ray diffraction experiments and related to the kinetics of the lattice tempera-

ture evolution in the surface region of the irradiated crystal.<sup>49</sup> Periodic oscillations of the diffraction peak positions have been recently probed with  $\sim 0.5$  ps resolution in electron diffraction experiments and related to the elastic vibrations of a free standing Al film irradiated with a femtosecond laser pulse.<sup>15,16</sup> Similar oscillations of the diffraction peak positions have been observed in simulations of 200 fs pulse laser excitation of a Ni film at low fluences, below the threshold for laser melting.<sup>50</sup> A discussion of the implications of the computational predictions on the shifts and splittings of the diffraction peaks for interpretation of experimental results obtained for polycrystalline targets and a fixed angle of incidence of the probe beam to the target surface is given in Sec. V.

#### D. Thermal effects

The decrease of the intensity of the diffraction peaks in the irradiated films can result from both structural changes and increasing thermal vibrations of the atoms. The latter contribution, related to the thermal smearing-out of the lattice planes, can be described by the Debye-Waller factor  $e^{-2M}$ , which relates the decrease of the peak intensity to the temperature evolution in the system,<sup>35</sup>

$$S(Q,t) - 1 = [S(Q,0 \text{ ps}) - 1] \frac{\exp[-2M(T(t),Q)]}{\exp[-2M(T(0 \text{ ps}),Q)]}. \quad (11)$$

The temperature dependence of the quantity  $M$  in the Debye-Waller factor can be expressed through the mean-square displacement (MSD)  $\langle u^2 \rangle$  of an atom vibrating around its equilibrium lattice position,

$$e^{-2M} = e^{-\frac{16\pi^2 \sin^2 \theta \langle u^2 \rangle}{3\lambda^2}} = e^{-\frac{\langle u^2 \rangle O^2}{3}}. \quad (12)$$

The MSD can be computed directly from atomic trajectories obtained in constant-volume MD simulations, performed for a range of temperatures corresponding to those measured in the simulations for laser excitation. The results of such calculations can be then used to predict the reduction of the peak heights in the laser excitation simulations due to the increase of the lattice temperature alone.

The results of the application of this approach to the simulation performed at an absorbed fluence of  $180 \text{ J/m}^2$  are shown in Fig. 8 for (111), (220), and (311) diffraction peaks. To make the connection between the thermal effects described by Eqs. (11) and (12) and the laser excitation simulations, we first calculate the average temperatures of the film at different times. The temperatures are then used to calculate the MSD and corresponding reduction of the peaks from the Debye-Waller factor, Eqs. (11) and (12). The results of the calculations are shown in Fig. 8 by dashed lines.

The heights of the peaks in the diffraction spectra calculated for the laser excitation simulation are shown in Fig. 8 up to 14 ps, whereas the results of the Debye-Waller calculations are shown up to 9 ps, the time when the average temperature of the film reaches  $1.25T_m = 1203 \text{ K}$  in the simulation of laser melting (above this temperature a fast homogeneous melting takes place within several picoseconds<sup>19-21</sup>

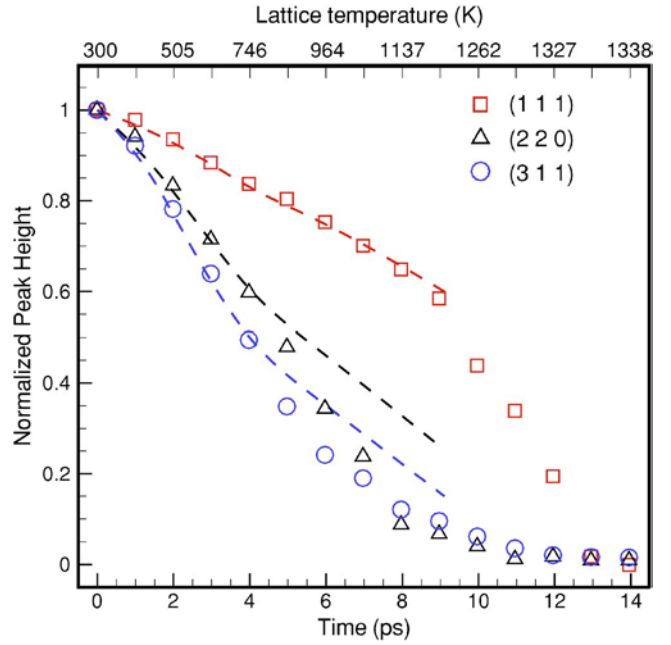


FIG. 8. (Color online) Normalized height of the (111), (220), and (311) peaks as a function of time after irradiation of a 20 nm Au film with a 200 fs laser pulse at an absorbed fluence of  $180 \text{ J/m}^2$ . All peak heights are normalized to their values at 0 ps ( $T=300 \text{ K}$ ). Dotted lines are calculated through the Debye-Waller factor up to the temperature of  $1.25 T_m$ , which corresponds to the limit of crystal stability. The values of the average temperature of the film at different times after the laser pulse are shown in the additional top  $x$  axis.

and the MSD for atomic vibration in a crystal cannot be obtained). There is a good agreement between the normalized peak heights and the Debye-Waller calculations up to  $\sim 4$  ps, when the average lattice temperature is  $\sim 750 \text{ K}$ . This agreement indicates that the observed reduction of the diffraction peaks during the first 4 ps is primarily due to the increased thermal vibration of the atoms. Starting from 5 ps, significant deviations from the Debye-Waller calculations can be observed for (220) and (311) peaks. As shown in Figs. 2, 3, and 4(a), the melting process starts only at  $\sim 10$  ps in this simulation and the onset of the deviation of the peak intensities from the Debye-Waller calculations can be attributed to the uniaxial film expansion discussed in Sec. IV C. As we can see from Fig. 3(b), the accumulated compressive pressure increases during the first picoseconds after the laser pulse and drives the expansion of the film. The expansion results in the distortion of the fcc lattice and associated tetragonal splitting of the (220) from the (202)/(022) and the (113) from the (311)/(131) peaks. The splitting is apparent in the structure function shown in Fig. 4(b) for 7 ps, and it starts to contribute to the decrease of the intensity of individual peaks from  $\sim 4.5$  ps. The (111) peak does not split and the data points are well described by the Debye-Waller calculations up to the onset of melting at about 9 ps (Fig. 8). During the melting process the (111) peak starts to overlap with a broad first peak characteristic of the liquid structure and the points for the (111) peak plotted in Fig. 8 for times starting from 10 ps correspond to the heights measured from

the background level provided by the broad liquid peak of the structure function (Fig. 4). A sharp drop of the intensity of the (111) peak is observed during the melting process, from 10 to 14 ps.

Thus, we can conclude that the reduction of the diffraction peaks heights is mainly defined by the increasing lattice temperature (Debye-Waller factor) during the first several picoseconds following the laser excitation, when the film does not have time to expand and is “inertially confined.”<sup>22</sup> As the film expands in response to the laser-induced thermoelastic stresses, the peak splitting due to the uniaxial lattice deformations starts to contribute to the reduction of the peaks. Finally, during the melting process the reduction of the height of the diffraction peaks is dominated by the destruction of the crystal order.

A similar analysis of the effect of the increasing lattice temperature on the diffraction peak intensities measured in the time-resolved electron diffraction study of laser-driven melting of thin Al films is presented in Ref. 12. The Debye equation and TTM are used in this work to predict the atomic mean square displacements and the temperature evolution, respectively. The conclusions from the analysis of the experimental data are in a good qualitative agreement with the computational results discussed above. The reduction of the diffraction peak heights initially follows the Debye-Waller calculation, with the onset of the deviations attributed to the loss of the crystalline order. A much shorter, as compared to the simulations, time for the beginning of the melting process, 1.5 ps, can be explained by a much stronger electron-phonon coupling in Al as compared to Au. Indeed, in a simulation performed for an Al film at irradiation conditions comparable to the experimental ones, we obtain an excellent quantitative agreement in both the time of the onset of melting and the duration of the melting process (see Sec. V).

### E. Real-space correlations

Structural changes during the laser-induced phase transformations can be further investigated by keeping track of the evolution of real-space correlation functions calculated for atomic configurations predicted in MD simulations. In particular, correlations in atomic positions can be expressed in the form of the reduced pair distribution function  $G(r)$ , which describes the deviation of the pair density function  $\rho(r)$ , defined by Eq. (6), from the average density  $\rho_0$ ,

$$G(r) = 4\pi r[\rho(r) - \rho_0]. \quad (13)$$

Experimentally,  $G(r)$  can be calculated by the sine Fourier transform of the structure function  $S(Q)$  and requires the ability to obtain the diffraction intensity of an adequate quality over a broad range of  $Q$ . This requirement presents a challenge for ultrafast time-resolved diffraction experiments that are often limited to the analysis of the diffraction signals obtained for fixed Bragg angles. The challenge of performing measurements for a range of scattering vectors can be met by increasing intensity of the x-ray or electron probes and accumulating the diffraction intensity over a large number of pulses.<sup>11,12,14,15</sup> In simulations, both  $\rho(r)$  and  $G(r)$  can be calculated directly from atomic configurations, using Eqs. (6) and (13).

An important advantage of  $G(r)$  is that its correlation peaks provide direct information on the structural coherence in the system. In real crystals,  $G(r)$  obtained from diffraction experiments oscillate around zero with peak amplitudes gradually decreasing with increasing  $r$  due to the crystal imperfections and the finite resolution of  $Q$  value in the measurement.<sup>38</sup> For disordered (liquid or amorphous) structures, the amplitude of  $G(r)$  oscillations decreases much faster, indicating the absence of long-range order.<sup>51</sup>

In Fig. 9 the reduced pair distribution function  $G(r)$  is presented for a simulation of a 20 nm Au film irradiated with a 200 fs laser pulse at an absorbed fluence of 180 J/m<sup>2</sup>. Before the laser excitation (0 ps),  $G(r)$  exhibits the characteristic features of the fcc crystalline structure. Each peak in  $G(r)$  corresponds to a specific interatomic distance between a pair of atoms in a perfect fcc structure. For example, the first peak in  $G(r)$  matches the distance between the nearest neighbors (2.89 Å) in a fcc crystal equilibrated at 300 K. Changes of  $G(r)$  during the fast homogeneous melting (see Fig. 4) are shown in Fig. 9(b). By comparing  $G(r)$  at 0 and 11 ps we can see that before the onset of melting the increasing lattice temperature results in a significant broadening of the correlation peaks and reduction of their intensities. Some of the peaks become completely obscured and merge with the neighboring ones, e.g., the peak corresponding to the second-neighbor shell cannot be identified in Fig. 9(b). The seeming “disappearance” of the correlation peaks before the onset of melting, however, does not correspond to any structural changes in the crystal but is just a consequence of the thermal broadening of all peaks, as demonstrated in the analysis presented at the end of this section. Despite the broadening, the peaks at 11 ps remain well defined for the range of interatomic distances considered in the calculation, confirming the presence of the long-range crystalline ordering in the atomic configuration. Between the times of 11 and 14 ps the peaks in the high- $r$  region disappear, reflecting a complete loss of the long-range order in the solid-to-liquid transition. The remained correlation peaks continue to broaden and diminish between the times of 14 and 40 ps [Fig. 9(c)], indicating that there are still some substantial changes in the short- or medium-range correlations in atomic positions. This observation suggests that within this period of time the liquid structure created after the collapse of crystalline state is still in a nonequilibrium state and retain some “memory” of the crystalline state.<sup>52</sup> The continuing increase of the lattice temperature [Fig. 3(a)] facilitates the destruction of the remaining medium-range ordering.

An alternative way of representing real-space correlations in atomic positions is provided by the radial distribution function (RDF)  $R(r)=4\pi r^2\rho(r)$ , from which coordination numbers corresponding to different neighbor shells can be determined by calculating the surface areas under the corresponding correlation peaks. The surface area can be found by the integration of  $R(r)$  with the integration limits corresponding to the local minima on the sides of the corresponding peak of the RDF. The RDF obtained in a simulation performed for a 20 nm Au film irradiated by a 200 fs laser pulse at 180 J/m<sup>2</sup> is shown for 0, 10, and 20 ps after the laser pulse in Fig. 10. For 0 ps, the first and second coordination

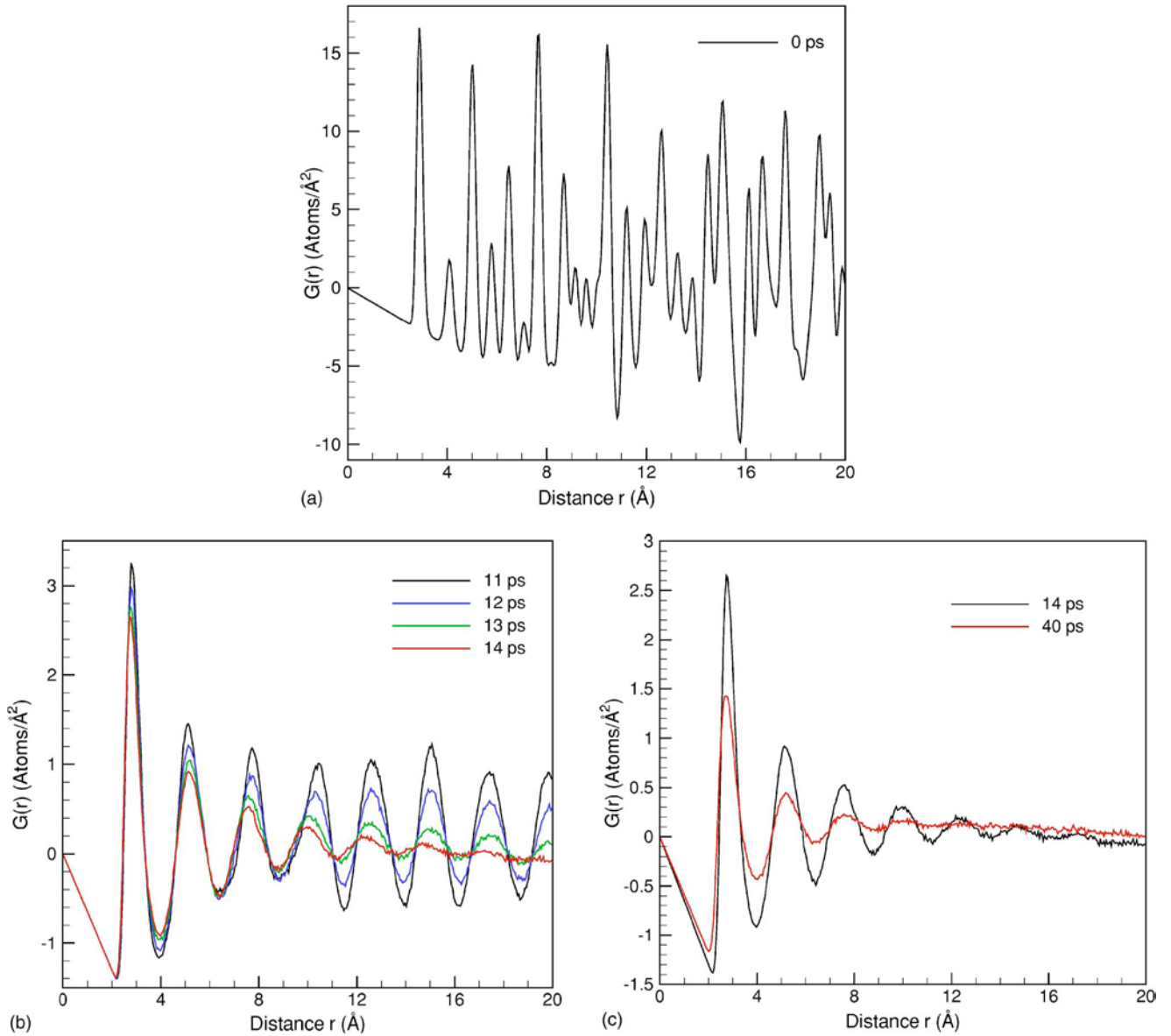


FIG. 9. (Color online) Reduced pair distribution function  $G(r)$  computed for atomic configurations obtained in a simulation of a 20 nm Au film irradiated with a 200 fs laser pulse at an absorbed fluence of  $180 \text{ J/m}^2$  at times of (a) 0, (b) 11–14, and (c) 14 and 40 ps.

numbers corresponding to the first and second peaks of the RDF are calculated to be 11.92 and 5.96. The values are less than the coordination numbers in a perfect fcc lattice, 12 and 6, due to the presence of the two free surfaces in our system, where atoms have a smaller number of neighbors. At 10 ps the first coordination number is determined to be  $12.1 \pm 0.4$  with the error value related to the uncertainty in defining the local minima in Fig. 10. This result indicates that, in agreement with visual picture of atomic configuration at 10 ps in Fig. 4(a), the local crystalline structure at this time is still preserved and most atoms still maintain 12 nearest neighbors. By the time of 20 ps the first coordination number decreases down to  $10.9 \pm 0.4$ , reflecting the destruction of the crystalline structure that is completed by this time [Fig. 4(a)]. A similar decrease of the first coordination number from 12 to 10 during the laser-induced melting process has been deduced from time-resolved electron diffraction measurements reported in Ref. 11 for a 20 nm Al film.

The output of MD simulations contains complete information on the atomic dynamics induced by laser excitation and allows for detailed investigation of the origin of the changes in the correlation functions discussed above and illustrated in Figs. 9 and 10. In particular, one question arises as to why the correlation peak corresponding to the second-neighbor shell in the fcc structure [Fig. 9(a)] completely disappears even before the onset of the melting process, e.g., the plots for 11 and 10 ps in Figs. 9 and 10, respectively. To answer this question and to better understand other aspects of the evolution of the correlation functions, we trace the motions of the first-, second-, and third-nearest neighbors of each atom in the original fcc lattice. By doing so, we decompose the RDF into separate contributions from the first three original coordination shells. The result of the decomposition, shown in Fig. 11, indicates that before 10 ps, on average, most atoms in the three coordination shells are still localized around their equilibrium positions. Significant broadening of

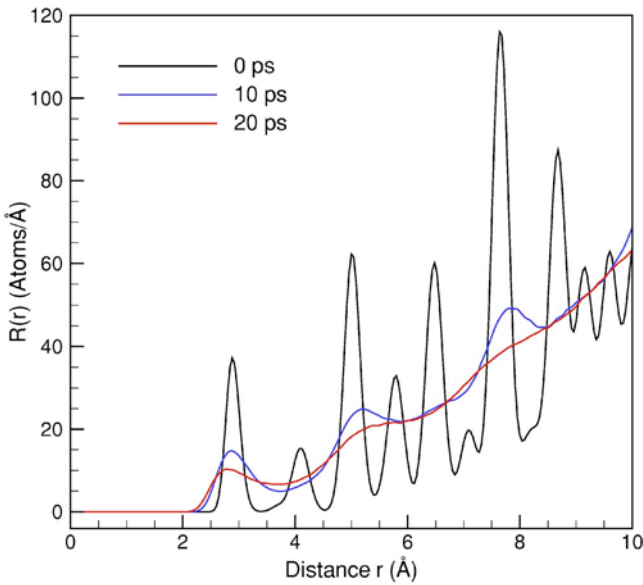


FIG. 10. (Color online) Radial distribution function  $R(r)$  computed for atomic configurations obtained in a simulation of a 20 nm Au film irradiated with a 200 fs laser pulse at an absorbed fluence of  $180 \text{ J/m}^2$  at times of 0, 10, and 20 ps. Coordination number  $N_c$  for the first coordination shell at  $\sim 2.89 \text{ \AA}$  can be obtained by integration of  $R(r)$  between the two local minima on either side of the first peak.

all the peaks, however, completely obscures the contribution from the peak corresponding to the second-neighbor shell [Fig. 11(d)], which shows itself only as a shoulder on the new second peak located at the position corresponding to the third-neighbor shell.

After the collapse of crystalline order, atoms gain the freedom to diffuse around. For the first-nearest-neighbor shell, atoms can only move outward, which leads to the long tail in the original first-nearest-shell contribution to the RDF at 14 and 20 ps [Fig. 11(a)]. The gradual disappearance of the original peak can be explained by the high mobility of atoms in the liquid state, leading to the loss of correlation between the positions of the nearest neighbors in the original fcc lattice. A similar gradual disappearance of the peak corresponding to the original third-nearest-neighbor shell is observed in Fig. 11(c), with some of the neighbors moving closer to the atoms of origin, others moving further away from them.

The evolution of the peak corresponding to the original second-nearest-neighbor shell is rather different from the ones of the first and third peaks [Fig. 11(b)]. By the time of 14 ps the second fcc peak completely disappears, splitting its intensity between the two peaks present in the liquid state. The fast disappearance of the second peak, also observed in a recent time-resolved electron diffraction study,<sup>11</sup> suggests that the interatomic distance corresponding to the second-nearest-neighbor shell in the fcc structure is not characteristic of the short-range order in the liquid structure. This interatomic distance appears in the octahedral atomic configuration characteristic of the close-packed crystals but is not typical for tetrahedral clusters responsible for the short-range order in one-component noncrystalline structures.<sup>53</sup> Thus, as soon as material melts, the atoms tend to escape from this

interatomic distance—octahedral configurations disappear and a broad second peak corresponding to the interatomic distances found in clusters with local tetrahedral and icosahedral short-range order<sup>54,55</sup> develops.

## V. CONCLUSION AND CONNECTIONS TO EXPERIMENTS

Computational analysis of the structure function and pair distribution function, performed for transient atomic configurations generated in MD simulations of fast laser-induced phase transformations, provides a connection between the atomic-level structural rearrangements and changes in the diffraction profiles. The laser-induced evolution of the diffraction peaks is found to be defined by the combination of the following three factors: (1) increasing amplitude of atomic vibrations associated with the fast temperature rise, (2) peak splitting due to the uniaxial lattice deformations, and (3) destruction of the crystal order in the melting process. The contribution of the increasing thermal atomic vibrations dominates during the first several picoseconds after the laser pulse and can be well described by the Debye-Waller factor. The film expansion in response to the laser-induced thermoelastic stresses results in shifts and splittings of the diffraction peaks, providing an opportunity for experimental probing of the ultrafast deformations. Finally, the onset of the melting process results in further reduction the diffraction peaks due to the destruction of the crystal order.

Two of the three contributions to the reduction of the diffraction peak intensity discussed above have been observed in recent time-resolved electron diffraction experiments.<sup>11–13</sup> For a 20 nm Al film irradiated at an excitation fluence of  $700 \text{ J/m}^2$ , the Debye-Waller calculations are found to be in a good agreement with experimental data for the first 1.5 ps, whereas further reduction of the height of the diffraction peaks has been attributed to the ultrafast melting that completes by the time of 3.5 ps after the laser pulse. No shifts in the positions of the diffraction peaks and no splitting of the peaks have been observed in this study as well as in time-resolved x-ray diffraction investigations of even faster nonthermal melting processes.<sup>5,6</sup> The absence of the shifts and splittings of the diffraction peaks can be related to the condition of the inertial stress confinement,<sup>22,56</sup> when the lattice heating and melting are taking place as constant-volume processes. In the case of the thermal melting, the time of the lattice heating is defined by the laser pulse duration  $\tau_p$ , and the time of the electron-phonon equilibration,  $\tau_{e\text{-ph}}$ , whichever is larger. The condition for the inertial stress confinement can be then formulated as  $\max\{\tau_p, \tau_{e\text{-ph}}\} \leq \tau_s \sim d/C_s$ , where  $d$  is the film thickness and  $C_s$  is the speed of sound in the film material. Due to the strong electron-phonon coupling in Al, the time of the electron-phonon equilibration (defined by the exponential fit of the time dependence of the energy transferred from the electrons to the lattice) is short,  $\tau_{e\text{-ph}} \approx 1.5 \text{ ps}$ , and fast homogeneous melting takes place before any significant expansion of the film can take place. Indeed, the results of the simulations of laser melting of a 20 nm Al film performed for experimental conditions reported in Ref. 11 show an ultrafast melting process within the first 3–4 ps with no peak shifts and splittings observed in

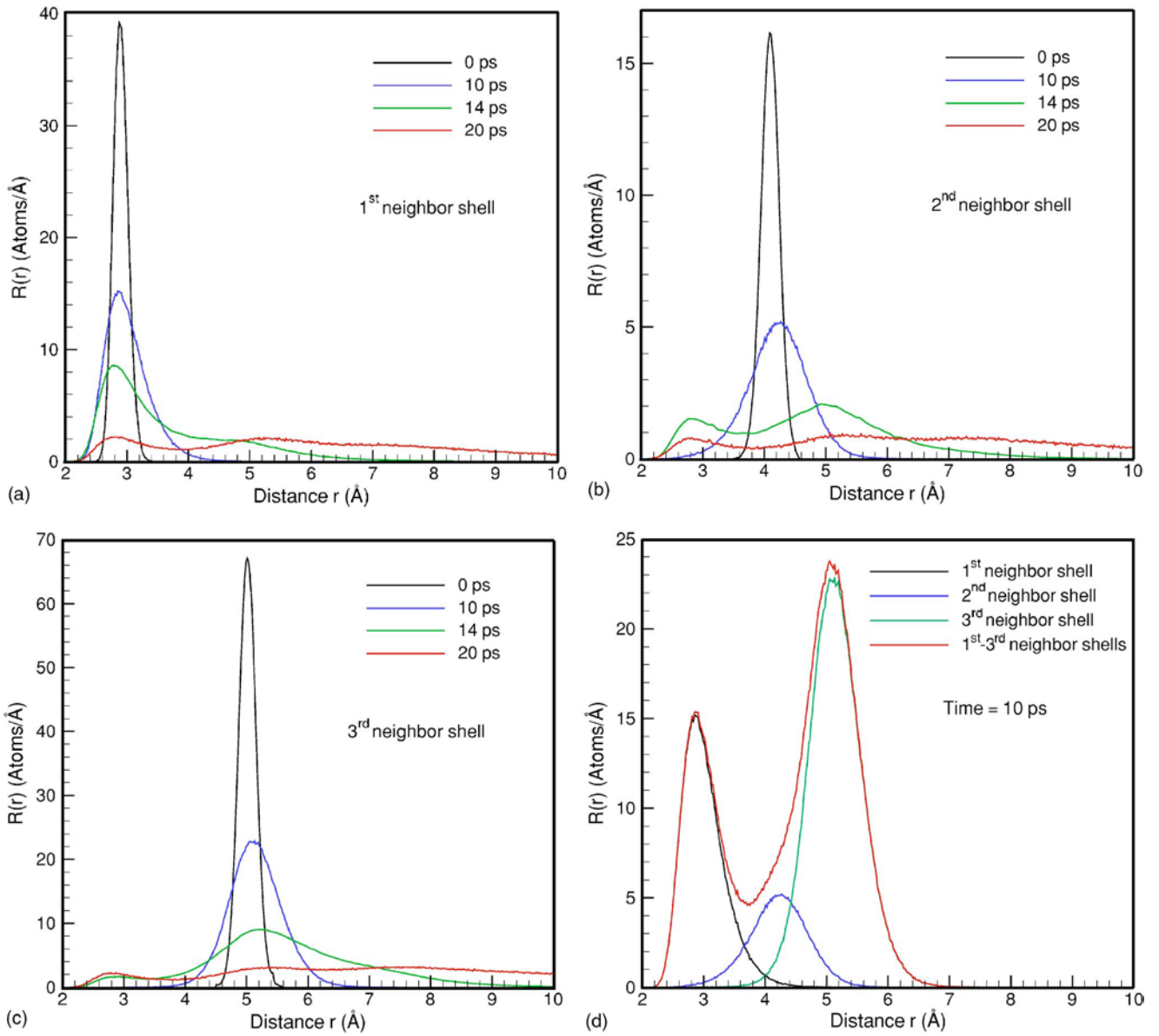


FIG. 11. (Color online) Decomposed radial distribution function  $R(r)$  of (a) first, (b) second, and (c) third coordination shells computed for atomic configurations obtained in a simulation of a 20 nm Au film irradiated with a 200 fs laser pulse at an absorbed fluence of  $180 \text{ J/m}^2$  at times of 0, 10, 14, and 20 ps. The peaks are calculated for atoms that belong to the corresponding coordination shells at the time of 0 ps. The data for the three coordination shells and their sum at 10 ps are shown in (d).

the diffraction spectra (Fig. 12). The time of the melting onset, 1.5 ps, the duration of melting process, and the evolution of the structure function are all in a very good quantitative agreement with experimental observations. In the case of even more rapid nonthermal melting occurring on a subpicosecond time scale<sup>5,6</sup> there is no doubt that the destruction of the crystal order occurs before any expansion of the material can take place.

In the simulations reported in this paper for Au films, a weak electron-phonon coupling in Au leads to a relatively slow heating of the film,  $\tau_{e-ph} \approx 15 \text{ ps}$ , whereas the small thickness of the film allows for a fast relaxation of thermoelastic stresses with  $\tau_s \approx 10 \text{ ps}$ . Actually, due to the presence of two free surfaces, the relaxation of the initial compressive pressure in a freestanding film takes place at an even

shorter time scale of  $\sim 5 \text{ ps}$  and is defined by the propagation of the two unloading waves from the free surfaces of the film [Fig. 3(b)]. As a result, the uniaxial expansion of the film precedes the onset of the structural transformation, and shifts and splittings of the diffraction peaks are observed in all simulations performed for Au films.

A clear separation of the time scales for lattice heating and melting has also been observed in the first time-resolved electron diffraction experiments performed for 20 nm Au films.<sup>13</sup> At an absorbed laser fluence of  $119 \text{ J/m}^2$ , well above the threshold for the complete melting of the film, the melting starts at about 7 ps after the laser pulse and is completed in about 3 ps. While the duration of the melting process is in an excellent agreement with the results of our simulations (Fig. 2), the time of the melting onset is significantly shorter

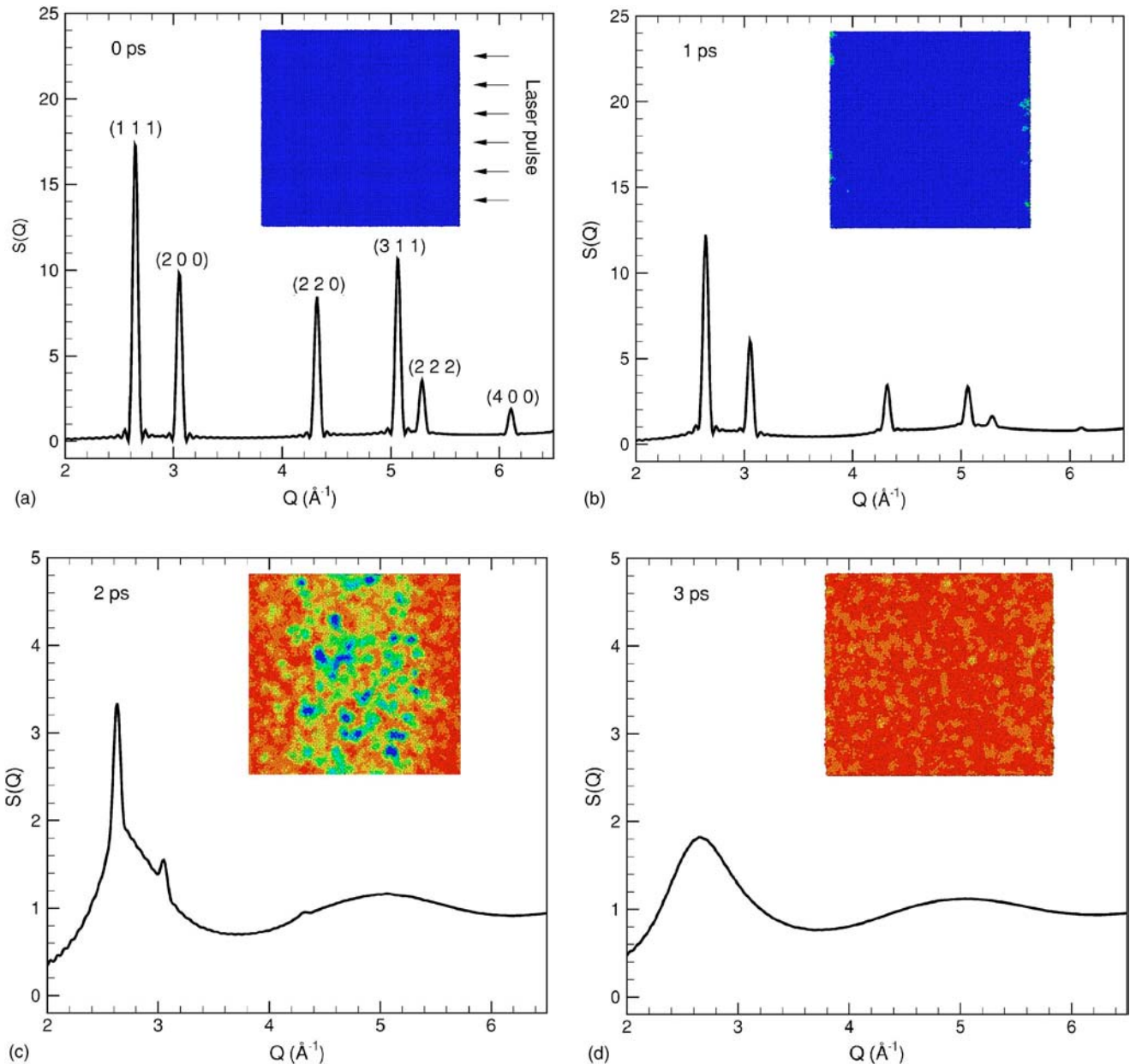


FIG. 12. (Color online) Structure functions calculated for atomic configurations obtained in a simulation of a 20 nm Al film irradiated with a 120 fs laser pulse at an absorbed fluence of  $84 \text{ J/m}^2$  at times of (a) 0, (b) 1, (c) 2, and (d) 3 ps. Insets show the corresponding snapshots of the atomic configurations, with the direction of the laser pulse shown in (a). Atoms are colored according to the local order parameter (blue atoms have local crystalline surroundings; red atoms belong to the liquid phase). The irradiation conditions are the same as in the experiment reported in Ref. 11 (incident fluence of  $700 \text{ J/m}^2$ , reflectivity of 88%).

in the experiment as compared to the simulations, 7 ps in experiment vs 17 ps in a simulation performed for comparable irradiation conditions. This quantitative discrepancy can be attributed to the assumption of the temperature-independent electron-phonon coupling constant used in this work. Indeed, recent calculations accounting for the contribution of the thermal excitation of the  $d$  band electrons to the electron heat capacity and electron-phonon coupling<sup>57</sup> significantly increase the rate of the lattice heating and show an excellent agreement with experimental results.

Note that the structure functions discussed in this paper (Figs. 4–7 and 12) are for single crystals and include the

information on all the lattice plane systems present in the crystal. In polycrystalline samples different orientations of crystallographic planes will be affected in a different way by the uniaxial expansion of the film and the structure function would exhibit broadening of the peaks instead of the splitting. In experiments performed with a fixed angle of incidence of the probe beam to the target surface, only the lattice planes that have the correct Bragg angle with the probe beam contribute to the measured diffraction spectrum. Splitting of the peaks can only be observed experimentally if probing is done at different incidence angles, so that different orientations of the same system of lattice planes with respect to the

direction of the uniaxial thermoelastic lattice expansion is probed. The maximum value of the peak shift is defined in this case not only by the extent of the film expansion but also by the orientation of the corresponding lattice planes with respect to the direction of the film expansion. The peak shift can be rather small if the planes having a small Bragg angle are probed in the transmission mode by an electron beam normal to the surface of the film.<sup>15,16</sup> Nevertheless, for a given direction of the probe beam, analysis of the peak shifts in time-resolved x-ray or electron diffraction experiments can provide valuable information on the characteristic time scale of the lattice heating and thermoelastic deformation<sup>15,16,49</sup> as well as on the role of the uniaxial deformation in laser-induced phase transformations.<sup>20</sup> A discussion of the simulation results for Ni films, where periodic oscillations of the diffraction peak positions are observed under low-fluence irradiation conditions (below the threshold for melting) and related to the laser-induced elastic vibrations of the film, is presented elsewhere.<sup>50</sup>

The emerging time-resolved electron and x-ray diffraction probe experiments are opening new opportunities for investigation of atomic dynamics in the time and spatial domains accessible for direct atomistic simulations. The results of the

simulations provide a direct link between the experimental observations and atomic-level structural changes in the irradiated material and help in interpretation of experimental data. In particular, the observed differences in the evolution of the diffraction profiles in the homogeneous and heterogeneous melting processes can, along with kinetics arguments, be instrumental in distinguishing between the two melting mechanisms. The shift and splitting of the diffraction peaks reflect the uniaxial thermoelastic lattice deformation of the film prior to melting and can be used for experimental probing of the laser-induced ultrafast deformations.

## ACKNOWLEDGMENTS

Z.L. would like to gratefully acknowledge the introduction to density correlation function analysis by Slava Kazimirov and Despina Louca. We also acknowledge Sean Agnew, Eduardo Bringa, Jason Dwyer, Dmitriy Ivanov, Dwayne Miller, and Klaus Sokolowski-Tinten for useful suggestions and discussions. Financial support of this work is provided by the NSF through Award No. CTS-0348503 and by the ONR through a subcontract from the Electro-Optics Center, Penn State University.

\*Email address: lz2n@virginia.edu;

URL: <http://www.faculty.virginia.edu/CompMat/>

<sup>1</sup>C. Guo, G. Rodriguez, A. Lobad, and A. J. Taylor, Phys. Rev. Lett. **84**, 4493 (2000).

<sup>2</sup>M. B. Agranat, S. I. Ashitkov, V. E. Fortov, A. V. Kirillin, A. V. Kostanovskii, S. I. Anisimov, and P. S. Kondratenko, Appl. Phys. A: Mater. Sci. Process. **69**, 637 (1999).

<sup>3</sup>L. Huang, J. P. Callan, E. N. Glezer, and E. Mazur, Phys. Rev. Lett. **80**, 185 (1998).

<sup>4</sup>O. P. Uteza, E. G. Gamaly, A. V. Rode, M. Samoc, and B. Luther-Davies, Phys. Rev. B **70**, 054108 (2004).

<sup>5</sup>A. Rousse, G. Rischel, S. Fourneaux, I. Uschmann, S. Sebban, G. Grillon, Ph. Balcou, E. Förster, J. P. Geindre, P. Audebert, J. C. Gauthier, and D. Hulin, Nature (London) **410**, 65 (2001).

<sup>6</sup>A. M. Lindenberg, J. Larsson, K. Sokolowski-Tinten, K. J. Gaffney, C. Blome, O. Synnergren, J. Sheppard, C. Caleman, A. G. MacPhee, D. Weinstein, D. P. Lowney, T. K. Allison, T. Matthews, R. W. Falcone, A. L. Cavalieri, D. M. Fritz, S. H. Lee, P. H. Bucksbaum, D. A. Reis, J. Rudati, P. H. Fuoss, C. C. Kao, D. P. Siddons, R. Pahl, J. Als-Nielsen, S. Duesterer, R. Ischebeck, H. Schlarb, H. Schulte-Schrepping, Th. Tschentscher, J. Schneider, D. von der Linde, O. Hignette, F. Sette, H. N. Chapman, R. W. Lee, T. N. Hansen, S. Techert, J. S. Wark, M. Bergh, G. Huldt, D. van der Spoel, N. Timneanu, J. Hajdu, R. A. Akre, E. Bong, P. Krejcik, J. Arthur, S. Brennan, K. Luening, and J. B. Hastings, Science **308**, 392 (2005).

<sup>7</sup>K. Sokolowski-Tinten, C. Blome, J. Blums, A. Cavalleri, C. Dietrich, A. Tarasevich, I. Uschmann, E. Förster, M. Kammler, M. Horn-von-Hoegen, and D. von der Linde, Nature (London) **422**, 287 (2003).

<sup>8</sup>M. Harbst, T. N. Hansen, C. Caleman, W. K. Fullagar, P. Jönsson, P. Sondhauss, O. Synnergren, and J. Larsson, Appl. Phys. A:

Mater. Sci. Process. **81**, 893 (2005).

<sup>9</sup>W. E. King, G. H. Campbell, A. Frank, B. Reed, J. F. Schmerge, B. J. Siwick, B. C. Stuart, and P. M. Weber, J. Appl. Phys. **97**, 111101 (2005).

<sup>10</sup>S. Williamson, G. Mourou, and J. C. M. Li, Phys. Rev. Lett. **52**, 2364 (1984).

<sup>11</sup>B. J. Siwick, J. R. Dwyer, R. E. Jordan, and R. J. D. Miller, Science **302**, 1382 (2003).

<sup>12</sup>B. J. Siwick, J. R. Dwyer, R. E. Jordan, and R. J. D. Miller, Chem. Phys. **299**, 285 (2004).

<sup>13</sup>J. R. Dwyer, C. T. Hebeisen, R. Ernstorfer, M. Harb, V. Deyirmenjian, R. E. Jordan, and R. J. D. Miller, Philos. Trans. R. Soc. London, Ser. A **364**, 741 (2006).

<sup>14</sup>J. Cao, Z. Hao, H. Park, C. Tao, D. Kau, and L. Blaszczyk, Appl. Phys. Lett. **83**, 1044 (2003).

<sup>15</sup>H. Park, S. Nie, X. Wang, R. Clinite, and J. Cao, J. Phys. Chem. B **109**, 13854 (2005).

<sup>16</sup>H. Park, X. Wang, S. Nie, R. Clinite, and J. Cao, Solid State Commun. **136**, 559 (2005).

<sup>17</sup>H. O. Jeschke, M. E. Garcia, M. Lenzner, J. Bonse, J. Krüger, and W. Kautek, Appl. Surf. Sci. **197-198**, 839 (2002).

<sup>18</sup>P. L. Silvestrelli, A. Alavi, M. Parrinello, and D. Frenkel, Phys. Rev. B **56**, 3806 (1997).

<sup>19</sup>D. S. Ivanov and L. V. Zhigilei, Phys. Rev. B **68**, 064114 (2003).

<sup>20</sup>D. S. Ivanov and L. V. Zhigilei, Phys. Rev. Lett. **91**, 105701 (2003).

<sup>21</sup>L. V. Zhigilei, D. S. Ivanov, E. Leveugle, B. Sadigh, and E. M. Bringa, Proc. SPIE **5448**, 505 (2004).

<sup>22</sup>E. Leveugle, D. S. Ivanov, and L. V. Zhigilei, Appl. Phys. A: Mater. Sci. Process. **79**, 1643 (2004).

<sup>23</sup>L. V. Zhigilei, Appl. Phys. A: Mater. Sci. Process. **76**, 339 (2003).

- <sup>24</sup>L. V. Zhigilei, E. Leveugle, B. J. Garrison, Y. G. Yingling, and M. I. Zeifman, Chem. Rev. (Washington, D.C.) **103**, 321 (2003).
- <sup>25</sup>S. I. Anisimov, B. L. Kapeliovich, and T. L. Perel'man, Zh. Eksp. Teor. Fiz. **66**, 776 (1974) [Sov. Phys. JETP **39**, 375 (1974)].
- <sup>26</sup>J. Hohlfeld, S.-S. Wellershoff, J. Gudde, U. Conrad, V. Jahnke, and E. Matthias, Chem. Phys. **251**, 237 (2000).
- <sup>27</sup>J. Hohlfeld, J. G. Müller, S.-S. Wellershoff, and E. Matthias, Appl. Phys. A: Mater. Sci. Process. **64**, 387 (1997).
- <sup>28</sup>X. W. Zhou, H. N. G. Wadley, R. A. Johnson, D. J. Larson, N. Tabat, A. Cerezo, A. K. Petford-Long, G. D. W. Smith, P. H. Clifton, R. L. Martens, and T. F. Kelly, Acta Mater. **49**, 4005 (2001).
- <sup>29</sup>Smithells' Metal Reference Book, 6th ed., edited by E. A. Brandes (Butterworths, London, 1983).
- <sup>30</sup>Y. S. Touloukian, *Thermophysical Properties of Matter, Vol. 4: Specific Heat: Metallic Elements and Alloys* (IFI/Plenum, New York, 1970).
- <sup>31</sup>Y. S. Touloukian, *Thermophysical Properties of Matter, Vol. 12: Thermal Expansion: Metallic Elements and Alloys* (IFI/Plenum, New York, 1975).
- <sup>32</sup>S. I. Anisimov and B. Rethfeld, Proc. SPIE **3093**, 192 (1997).
- <sup>33</sup>B. Rethfeld, A. Kaiser, M. Vicanek, and G. Simon, Phys. Rev. B **65**, 214303 (2002).
- <sup>34</sup>N. W. Ashcroft and N. D. Mermin, *Solid State Physics* (Holt, Rinehart and Winston, New York, 1976).
- <sup>35</sup>B. E. Warren, *X-Ray Diffraction* (Addison-Wesley, Reading, MA, 1969).
- <sup>36</sup>J. M. Cowley, *Electron Diffraction Techniques* (Oxford Science Publications, Oxford, 1992), Vol. 1.
- <sup>37</sup>Z. L. Wang, *Elastic and Inelastic Scattering in Electron Diffraction and Imaging* (Plenum Press, New York, 1995).
- <sup>38</sup>T. Egami and S. J. L. Billinge, *Underneath the Bragg Peaks: Structural Analysis of Complex Material* (Elsevier, Amsterdam, 2003).
- <sup>39</sup>P. M. Derlet, S. Van Petegem, and H. Van Swygenhoven, Phys. Rev. B **71**, 024114 (2005).
- <sup>40</sup>R. Lovell, G. R. Mitchell, and A. H. Windle, Acta Crystallogr., Sect. A: Cryst. Phys., Diffra., Theor. Gen. Crystallogr. **35**, 598 (1979).
- <sup>41</sup>P. F. Peterson, E. S. Bozin, T. Proffen, and S. J. L. Billinge, J. Appl. Crystallogr. **36**, 53 (2003).
- <sup>42</sup>G. Gutiérrez and B. Johansson, Phys. Rev. B **65**, 104202 (2002).
- <sup>43</sup>E. A. Lorch, J. Phys. C **2**, 229 (1969).
- <sup>44</sup>K. Laaziri, S. Kycia, S. Roorda, M. Chicoin, J. L. Robertson, J. Wang, and S. C. Moss, Phys. Rev. B **60**, 13520 (1999).
- <sup>45</sup>L. V. Zhigilei and D. S. Ivanov, Appl. Surf. Sci. **248**, 433 (2005).
- <sup>46</sup>K. A. Jackson, Interface Sci. **10**, 159 (2002).
- <sup>47</sup>B. Rethfeld, K. Sokolowski-Tinten, D. von der Linde, and S. I. Anisimov, Phys. Rev. B **65**, 092103 (2002).
- <sup>48</sup>T. M. Holden, J. H. Root, R. A. Holt, and M. Hayashi, Physica B **213**, 793 (1995).
- <sup>49</sup>P. Chen, I. V. Tomov, and P. M. Rentzepis, J. Chem. Phys. **104**, 10001 (1996).
- <sup>50</sup>Z. Lin and L. V. Zhigilei, in *Proceedings of the 8th International Conference on Laser Ablation (COLA'05)*, J. Phys. Conference Series (to be published).
- <sup>51</sup>V. Petkov, S. J. L. Billinge, S. D. Shastri, and B. Himmel, Phys. Rev. Lett. **85**, 3436 (2000).
- <sup>52</sup>Y. A. Bazin and B. A. Baum, Izv. Vyssh. Uchebn. Zaved., Chern. Metall. **8**, 36 (1996) [Steel Transl. **26**, 43 (1996)].
- <sup>53</sup>V. A. Likhachev, A. I. Mikhailin, and L. V. Zhigilei, Philos. Mag. A **69**, 421 (1994).
- <sup>54</sup>T. Schenk, D. Holland-Moritz, V. Simonet, R. Bellissent, and D. M. Herlach, Phys. Rev. Lett. **89**, 075507 (2002).
- <sup>55</sup>G. X. Li, Y. F. Liang, Z. G. Zhu, and C. S. Liu, J. Phys.: Condens. Matter **15**, 2259 (2003).
- <sup>56</sup>G. Paltauf and P. E. Dyer, Chem. Rev. (Washington, D.C.) **103**, 487 (2003).
- <sup>57</sup>Z. Lin and L. V. Zhigilei, in *High-Power Laser Ablation VI*, Proc. SPIE (to be published July 2006).